Journal of Volcanology and Geothermal Research 465 (2025) 108351

Contents lists available at ScienceDirect

Journal of Volcanology and Geothermal Research

journal homepage: www.journals.elsevier.com/journal-of-volcanology-and-geothermal-research

# Simulation of the 2012 Te Maari debris avalanche: Insight into the failure mechanics and the role of the hydrothermal system

Juliette Vicente [a,*], Stuart Mead [a], Gabor Kereszturi [a], Craig Miller [b]

[a] Volcanic Risk Solutions, Institute of Agriculture and Environment, Massey University, Private Bag 11222, Palmerston North, 4442, New Zealand
[b] GNS Science, Wairakei Research Centre, Private Bag 2000, Taupo, 3352, New Zealand

## ARTICLE INFO

*Keywords:*
Slope failure
Debris avalanche
Finite element method
Pore pressure
Infiltration
Multiple-stage failure

## ABSTRACT

Composite volcanoes consist of alternating layers with varying mechanical properties, which contribute to the instability of the flanks. This instability can lead to the onset of mass flows down volcanic slopes, posing significant risks to nearby populations and infrastructures. Tongariro, an active andesite volcano, experienced one of New Zealand's most recent debris avalanches at the Upper Te Maari crater on August 6, 2012. This debris avalanche, initiated simultaneously with a small-magnitude earthquake, released a volume of $7 \times 10^5$ m$^3$ of material from the source, which by unloading the pressurised vapour-dominated hydrothermal system, led to a phreatic eruption. This paper aims to better constrain the preparatory and triggering factors, along with the failure mechanics, that led to the 2012 debris avalanche. To achieve this, we applied slope stability finite-element modelling to assess the volcanic slope's sensitivity to varying groundwater, seismic and mechanical conditions. Model results closely match the observed failure when considering the strength of hydrothermally altered rocks subjected to an increased pore pressure at shallow depth. We found that even a relatively minor rise in pore pressure, ≈ 250 kPa in the upper layers, could replicate the observed failure at Te Maari. Our simulations also reveal that this debris avalanche might be a multiple-stage failure involving the progressive sliding of two distinct blocks. These findings enhance our understanding of Tongariro's structure and improve hazard assessments for future potential collapses at Tongariro and other New Zealand volcanoes.

## 1. Introduction

Volcanoes form complex structures through the accumulation of alternating layers of lava, pyroclastic material, and endogenous growth (Ball et al., 2018; Heap et al., 2021). The accumulation of these materials not only steepens the edifice's slopes, but also results in physical and mechanical variability from one layer to another (Heap et al., 2021). This broad range of physical and mechanical characteristics (e.g. density, alteration potential, strength) favours the instability of volcanic flanks, leading to mass flow events such as lahars or volcanic debris avalanches. The latter are very frequent on the geological time scale, with approximately a thousand volcanic debris avalanches identified to date for 600 volcanoes, each exhibiting diverse failure types, modes of emplacement, and associated risks (Siebert and Roverato, 2021). Debris avalanche processes are time dependent phenomena (Flageollet, 1996; Qin et al., 2001; Van Asch et al., 2007) that progress through distinct phases (pre-failure, failure, post-failure), each characterised by different timescales and controlling factors. The pre-failure phase, marked by gradual weakening of the edifice, often unfolds over extensive timescales, from years to millennia. This leads into the failure phase, a transient event lasting milliseconds to seconds, where a volume of material detaches from the volcano along a developing shear surface. The most significant risks arise during the post-failure phase, where the failed mass flows down the slope, a process that may last minutes to weeks (Van Asch et al., 2007). If this flow is characterised by an extreme mobility, it can significantly impact nearby populations and infrastructures (Pudasaini and Miller, 2013). High mobility in volcanic debris avalanches results from fluidisation phenomena which can substantially increase runout distances, even for smaller-volume debris avalanches (Siebert and Roverato, 2021; McGuire, 1996; Hungr et al., 2008). Additionally, numerous volcanic flank collapses are associated with magmatic eruptions (Siebert et al., 2011; Heap et al., 2021), demonstrating their potential to trigger secondary catastrophic events, such as the 1980 Mount St Helens (Glicken, 1996) and the 1956 Bezimianny eruptions (Belousov et al., 2007). Both share similarities including a flank collapse that triggered an instantaneous pressure drop on the volcano, followed by a volcanic blast (Siebert and Glicken, 1987; Sousa and Voight, 1995; Glicken, 1996; Belousov, 1996; Belousov et al., 2007; Siebert and Roverato, 2021).

---

* Corresponding author.
*E-mail address:* j.vicente@massey.ac.nz (J. Vicente).

https://doi.org/10.1016/j.jvolgeores.2025.108351
Received 4 December 2024; Received in revised form 14 April 2025; Accepted 3 May 2025

Flow initiation and subsequent mechanics are strongly influenced by failure conditions. Volcanic slope instabilities are promoted by a combination of preparatory and triggering factors (Van Asch et al., 2007), often related to volcanic activity. Preparatory factors are contingent on the pre-failure phase, during which progressive structural changes occur, leading to the weakening of the slope. These changes may result from the cumulative effect of long-term factors, such as groundwater circulation and hydrothermal alteration (Mordensky et al., 2018b; Kennedy et al., 2020; Schaefer et al., 2023; Mordensky et al., 2022), as well as short-term influences such as climatic events and magmatic intrusions. Triggering factors of slope movements are transient (Crozier, 1986; Leroueil, 2001; Van Asch et al., 2007) and are responsible for either decreasing the shearing resistance of the material and/or increasing the shear stress (Duncan et al., 2014). These triggering factors include internal overpressures linked to pressurised magma (Schaefer et al., 2023), hydrothermal fluids (Reid, 2004) and/or gases (Voight and Elsworth, 2000); seismic activity (Sherburn et al., 1999; Calder et al., 2002; Mordensky et al., 2022) or exogenous processes such as heavy rainfall (Carn et al., 2004) or snow melting (Pierson et al., 1990). Steep slopes (Siebert, 1984; Moon et al., 2005; Miller and Williams-Jones, 2016) and the presence of a hydrothermal system are often identified as significant contributors to volcano instability by promoting both preparatory factors (e.g. alteration of material properties; Van Wyk de Vries et al. 2000, Reid et al. 2001, del Potro and Hürlimann 2009) and triggering factors (e.g. shallow seismicity, fluid redistribution, and pore pressure changes ; Reid 2004, Cecchi et al. 2004, Ball et al. 2018, Rosas-Carbajal et al. 2016, Heap et al. 2021). The presence of hydrothermally altered material has been demonstrated to weaken slopes by precipitating weaker secondary minerals, such as sulfates and phyllosilicates, thus promoting flank collapses (e.g. Reid et al. 2001, del Potro and Hürlimann 2009, Ball et al. 2015, Siratovich et al. 2016, Bouligand et al. 2016, Mordensky et al. 2019, Heap et al. 2021, Kereszturi et al. 2021). In addition to these mineralogical changes, hydrothermal alteration can also reduce porosity and permeability (e.g. by the precipitation of clays, silica polymorphs, sulfides and sulfates), leading to increased pore pressure and consequently promoting instabilities (Reid, 2004; Heap et al., 2019; Ball et al., 2018). Moreover, uncapping a pressurised hydrothermal system can lead to subsequent explosive behaviour (Siratovich et al., 2016; De Moor et al., 2019; Heap et al., 2021; Kennedy et al., 2020; Mick et al., 2021). Consequently, a thorough analysis of these pre-failure weakening factors and the failure mechanics is essential to assess the hazards associated with the subsequent post-failure movement.

Numerical modelling can be used as a tool for examining the physics and impacts of the different phases of debris avalanches. Slope stability models have been extensively used to investigate the mechanics of major collapse events and assess the slope response to changes in material properties (Kereszturi et al., 2021; Schaefer et al., 2015; Wallace et al., 2022), groundwater conditions (Ball et al., 2018; Mordensky et al., 2022) or external loads (Iverson, 1995). Continuum numerical methods such as finite element method (FEM) have demonstrated their effectiveness in assessing failure modes by allowing the calculation of stress and strain distribution (Duncan, 1996; Hammah et al., 2005; Schaefer et al., 2023; Wallace et al., 2022) and accurately capturing the complex behaviour of slopes composed of heterogeneous and anisotropic materials (Duncan, 1996). FEM analysis enables a detailed visualisation of the development of failure mechanisms under various disturbance factors (Schaefer et al., 2023), without requiring assumptions about the type, shape, or location of sliding surfaces.

In this study, we develop a stability model using the FEM to investigate the mechanical and groundwater scenario involved in the failure that occurred at Te Maari, Tongariro (New Zealand) in 2012. The succession of events (Section 2.2) suggests that the failure is linked to the presence of an active vapour-dominated shallow hydrothermal system (Miller et al., 2018) beneath the edifice (Walsh et al., 1998; Hill et al., 2015; Miller and Williams-Jones, 2016). The Te Maari case study, enriched with a multitude of various pre- and post-event geophysical data (e.g. topographic, gravimetric, magnetic, hyperspectral) provides well-constrained information and serves as an instructive case to thoroughly explore failure processes in hydrothermal systems over a complete timespan. Here, we tested the sensitivity of the slope to various groundwater, seismic and mechanical scenarios, allowing for a better characterisation of the preparatory and triggering factors involved in the 2012 event. We then discuss the influence of these factors on the failure mechanics and highlight implications for future volcanic hazard assessments.

## 2. Tongariro and the 6th of August 2012 debris avalanche

Tongariro is a multi-centre composite volcano (Leonard et al., 2021) covering an area of approximately 65 $km^2$, located at the southern boundary of the Taupo Volcanic Zone (TVZ). Volcanism at Tongariro is characterised by frequent, low-volume (0.1–1 $km^3$) eruptions with compositions ranging from basaltic andesite to dacite (Hobden et al., 1996; Nakagawa et al., 1998; Hobden et al., 2002; Shane et al., 2017). The volcanic complex consists of at least 15 overlapping vents that were formed during 6 episodes of major cone formation (Hobden et al., 1999). Since the first eruption c. 275 kyr ago in the Lower Tama Lake area (Hobden et al., 1996), the edifice has undergone many geomorphic changes, including glacial erosion (Topping, 1974; Cole et al., 2018; Leonard et al., 2021; Eaves and Brook, 2021) and later eruptions from new vents, making it difficult to identify old vents. Geomorphic changes due to volcanic mass flows (pyroclastic density currents, lahars, debris avalanches, etc.) are very rare in the history of Tongariro, compared to its neighbour, Ruapehu. However, 5 lahar-type deposits have been identified as resulting from the activity of the Tongariro volcanic complex between 26 and 11 kyr ago, in the northeast part of the massif (Cronin et al., 1997; Procter et al., 2014). These deposits are mainly preserved 10–30 km from the source and are attributed to the remobilisation of loose pyroclastic deposits. To the northwest, Lecointre et al. (2002), identified and mapped the Te Whaiau Formation, which consists of a large debris avalanche deposit (0.5 $km^3$) emplaced between 55 and 60 kyr ago, initiated as a wet debris avalanche that transformed downstream into a single cohesive debris flow. On the northern flanks, Topping (1974) mapped a series of proximal lahar deposits, the Mangatipua Formation, that are associated with the eruption of Te Maari craters in November 1892. The present morphology of the volcanic edifice is therefore the result of gravitational collapses, as well as the retreat of the glaciers, which greatly contributed to the generation of lahars by providing large quantities of water and exposing the loose, unconsolidated volcanic material in the valleys (Procter et al., 2014). Since the Mangatipua Formation, no debris flows, landslides, or lahars were observed on Tongariro until 2012.

### *2.1. Hydrothermal system of Tongariro*

The hydrothermal system of Tongariro, identified as a large, deep demagnetised and low-density region by Miller and Williams-Jones (2016), extends from north of Ngauruhoe to Upper Te Maari, reaching the basement rocks at approximately 2 km depth. It is predominantly vapour-dominated (Miller et al., 2018) with localised condensate zones, as revealed by multiple electrical geophysical studies (Walsh et al., 1998; Hill et al., 2015; Miller et al., 2018; Heise et al., 2024). A low-resistivity layer at approximately 1000 m a.s.l has been interpreted as a condensate layer several hundred metres thick, with Ketetahi Hot Springs acting as one of its major outflows (Walsh et al., 1998; Hill et al., 2015). However, a more recent groundwater study conducted by Miller et al. (2018) confirmed the presence of a binary hydrothermal system dominated by vapour and liquid zones but also revealed that the system is highly segmented, with irregularly distributed vapour and condensate regions. This complex distribution likely explains the spatially heterogeneous observations of surface unrest indicators prior to the 2012 Te Maari eruption (Miller et al., 2018).

Due to the presence of this extensive, complex, active hydrothermal system, rocks constituting Tongariro's edifice undergo significant physico-chemical alterations. The interaction between host rocks and hot acidic fluids results in the precipitation of secondary minerals, often with lower densities, such as sulfides (marcasite), phyllosilicates (kaolin-, smectite-, mica- and chlorite-group minerals, montmorillonite), sulfates (alunite, jarosite, barite, gypsum, anhydrite), silica polymorphs (opal, trydimite, cristobalite), and native sulfur. These alterations, affecting the physical characteristics of the rocks, significantly influence the mechanical response and failure mode (Reid et al., 2001; Heap et al., 2015). With the volume of hydrothermally altered rock within Tongariro edifice estimated at about 20 $km^3$ (Miller and Williams-Jones, 2016), it is important to characterise hydrothermal zones for volcanic hazard assessment, as they could serve as sources for future debris avalanches.

### 2.2. The 6th of August 2012 debris avalanche and eruption

The most recent eruptions of Tongariro occurred on August 6, 2012, and November 21, 2012, at Upper Te Maari Crater (Procter et al., 2014; Jolly et al., 2014) and are linked to the presence of the hydrothermal system. The August 6 event featured a complex eruption sequence, including a small debris avalanche, a multiple-pulse phreatic eruption and the formation of a chasm in a fissure-like form (Fig. 1) about 300 m from the main eruption vent (Jolly et al., 2014).

Unrest began on July 13, 2012, marked by volcano-tectonic and high-frequency repeating earthquakes occurring in three distinct swarms: July 12–13, July 17–20, and July 29–30, 2012 (Hurst et al., 2014). This unrest was also marked by an increase in long-period (LP) earthquakes which are associated with a source mechanism typically ascribed to fluid resonance in the volcano conduit and fractures (Clarke et al., 2021). On 6 August 2012, two local earthquakes of approximately magnitude 1.8 $M_L$ were recorded at 23:49:06 (UTC+12) and 23:49:21 (UTC+12). Jolly et al. (2014) located the first earthquake directly within the head wall of the debris avalanche scar (Fig. 1), suggesting it triggered the collapse of approximately $7 \times 10^5$ $m^3$ of material from the northern flank of the volcano (Procter et al., 2014). This first earthquake was then interpreted as concomitant with the onset of the debris avalanche (Jolly et al., 2014). The second earthquake was followed by a low amplitude persistent tremor for about two minutes, interpreted as the signature of the debris avalanche, increasing in amplitude and culminating in a series of explosive pulses beginning at 23:52:18 (UTC + 12), marking the onset of the phreatic eruption (Jolly et al., 2014). The eruption is therefore presumed to result from depressurisation due to the unroofing of the hydrothermal system (Procter et al., 2014). The end of this eruption phase was marked by the generation of an eruptive column about 10 km high (Crouch et al., 2014). Intense degassing followed this eruption (Christenson et al., 2013) until November 21, when a smaller eruption that caused localised ash fallout and short-distance pyroclastic flows (Jolly et al., 2014) occurred.

The debris avalanche transformed into a cohesive debris flow that travelled more than 2 km from the source and covered an area of 151 000 $m^2$ (Fig. 1), following the existing topography of the Mangatipua Stream (Procter et al., 2014). Deposits are characterised by a mixture of hydrothermally altered clasts and agglutinated scoria in a fine clay-rich matrix.

## 3. Method

In this study, finite element slope stability simulations are performed using the 2D finite-element analysis (FEA) software RS2. These analyses examine the influence of the hydrothermal system on rock properties and pore pressure distribution within the edifice, offering insights into its impact on failure mechanics.

FEM discretises the rock mass into smaller polygonal sections, calculating stress and strain at each node when subjected to external loads. This approach allows for a more detailed representation of the internal stress distribution and deformation characteristics (Duncan, 1996), which is particularly useful in the Te Maari case study due to the slope's heterogeneous material properties, including highly deformable altered materials (Fig. 3). The failure surface in each scenario is determined through iterative techniques (Duncan, 1996), and corresponds to areas of the edifice where the shear strength is no longer able to maintain the shear stress applied (Wong, 1984). To calculate the critical shear strength of the material and therefore quantify the stability at Te Maari, we used the shear stress reduction (SSR) method (Zienkiewicz et al., 1975; Matsui and San, 1992; Dawson et al., 1999; Zheng et al., 2006; Chang and Huang, 2005). This method iteratively reduces strength parameters until the FEM model fails to converge, which is interpreted as failure (Duncan, 1996). The ratio of initial strength parameters to reduced strength parameters at failure is then determined, expressed as the critical shear reduction factor (SRF).

The general inputs required to conduct these FEM stability analyses are the geometry of the edifice, the mechanical response of the materials (e.g. failure criterion, strength parameters), the groundwater conditions and the external forces (e.g. seismic loading).

### 3.1. Model geometry

Detailed topographic and subsurface information about the Te Maari edifice are required as boundary conditions for the finite element analysis (FEA). Pre- and post-event DEM data are available, allowing a precise description of erosion processes and debris avalanche deposition (Procter et al., 2014). A difference map between these elevation models allowed the estimation of the debris avalanche source outline (Fig. 1) and initial volume, ranging from $6,83 \times 10^5$ to $7,74 \times 10^5$ $m^3$ (Procter et al., 2014).

Topography for the FEA is based on a 10 m resolution pre-event DEM provided by GNS Science. This dataset was derived from 20 m contours of the New Zealand LINZ national database originally obtained through stereo photogrammetry in 1975 (Procter et al., 2014). The post-topography is derived from a 1 m resolution post-event DEM obtained through a LiDAR survey conducted in November 2012 (Procter et al., 2014).

#### 3.1.1. Subsurface geometry of the rock units

While most of the groundwater studies (Walsh et al., 1998; Hill et al., 2015; Miller and Williams-Jones, 2016; Miller et al., 2018) encompassed the entire volcanic edifice, the 2012 debris avalanche, constituting a small and shallow event, is inherently very localised. Consequently, the resolution of these studies does not allow for an accurate identification of the heterogeneities within the shallowest layers of the edifice near Te Maari. As a result, the geometry of our model is guided by interpretations of these geophysical data, rather than direct adoption of the geophysical models.

Our approach first used the image classification of Kereszturi et al. (2018) which integrates data from several surveys, an airborne hyperspectral survey conducted in April 2016 (Kereszturi et al., 2018), and the LiDAR survey of November 2012 used to generate the 10 m post-event DEM. Field studies were also conducted in early 2017 (Kereszturi et al., 2018) to investigate the lithologies located around Te Maari craters. This classification effectively delineates the surface lithology, particularly highlighting hydrothermally altered rocks in-situ at the surface. The area of interest for our study is the Upper Te Maari crater, wherein a highly localised zone of in situ alteration is observed (Fig. 1). The identification of surface alteration in this area facilitates an initial estimation of sub-surface properties.

Gravity data collected by Miller and Williams-Jones (2016) were then used to estimate the three dimensional extent of the altered material. Results revealed a local negative complete Bouguer Anomaly

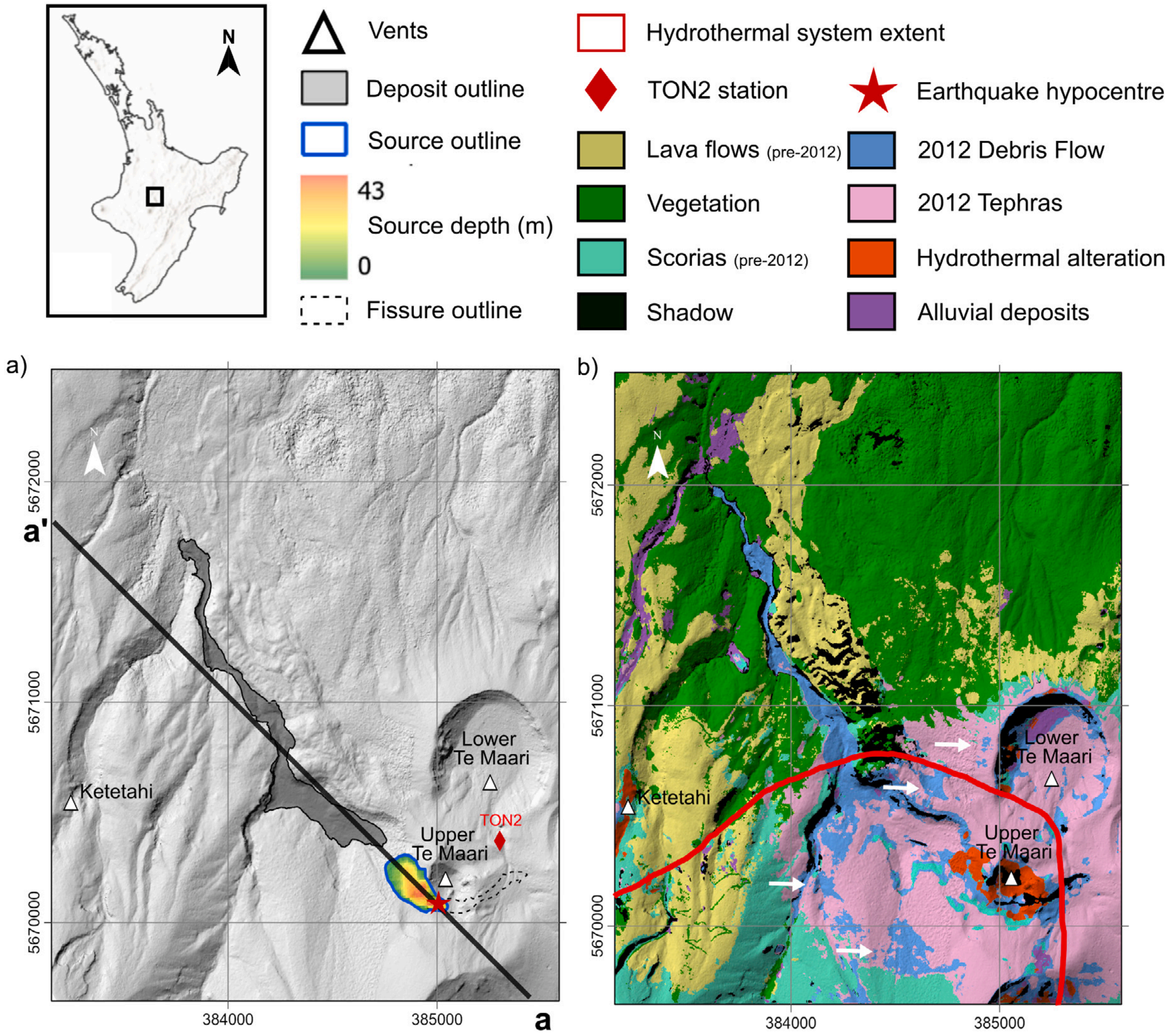

**Fig. 1.** (a) Location of the source and deposits of the 2012 debris avalanche. The blue line outlines the source location and the failure depth for each pixel is represented. The dashed line outlines the phreatic eruption fissure. The red star represents the earthquake hypocentre from Jolly et al. (2014) (referred to as EQ (HF) 1 in their study), while the red diamond marks the location of the TON2 station. Profile aa' is used for 2D slope stability simulations. (b) Simplified geological map obtained from the hyperspectral-based image classification of Kereszturi et al. (2018) (overall accuracy of 85%, misclassified areas are highlighted by white arrows). The red line outlines the extent of the hydrothermal system from Miller and Williams-Jones (2016).

at Te Maari, indicating a low-density region and suggestive of the presence of hydrothermally altered rocks. This low-density region was delineated within a density isosurface of 2250 kg/m$^3$ (Fig. 1, Miller and Williams-Jones 2016). Although this model can clarify the extent at depth of the hydrothermal system identified in Kereszturi et al. (2018), the surface alteration may not correspond to that found at depth. Miller and Williams-Jones (2016) suggest that the highly altered surface zones likely surround a core of less altered rocks that extends to depth. Additionally, the relatively coarse resolution of the model is sufficient to characterise the entire hydrothermal system across the volcanic complex but lacks the necessary resolution to fully define alteration at specific areas of the volcano.

The 2012 deposits originate from a shallow altered zone (Kereszturi et al., 2018) and do not exhibit significant differences in geomechanical properties (Procter et al., 2014). Therefore, the source of the debris avalanche can be assumed from a single altered unit. In that sense, and following other studies (e.g. Wallace et al. 2022), we simplified our FEA models into two geological units (Fig. 2) :

- The altered unit encompassing rocks exhibiting signs of hydrothermal alteration.
- The unaltered unit comprising rocks that are not or only slightly affected by alteration processes.

This assumption is sufficient to evaluate the general influence of altered geomechanical properties on the pre-event edifice stability.

We assume the 3D alteration extent as constrained on the surface using the hyperspectral classification of Kereszturi et al. (2018), and at depth using the low-density isosurface of Miller and Williams-Jones (2016). These surfaces were merged using a convex hull, creating the smallest convex volume enclosing all points from both surfaces. The resulting volume (Fig. 2b) was assigned to the altered unit, and the rest of the model to the unaltered unit. From this 3D geometry (Fig. 2b), we extracted a 2D profile, aa' (Fig. 2c), following the major axis of the observed failure, which is used for our numerical simulations.

### 3.2. Material mechanical response

#### 3.2.1. Generalised Hoek–Brown criterion

To predict failure under triaxial stresses, our analyses employ the Generalised Hoek–Brown (GHB) criterion, which accounts for the discontinuities and surface conditions of the rock masses (Hoek and Brown, 1980; Hoek et al., 2002; Hoek, 2005).

This criterion comprises a set of non-linear equations, derived from a combination of the work by Hoek (1968) on the brittle failure of intact rock and Brown (1970) on the behaviour of jointed rock

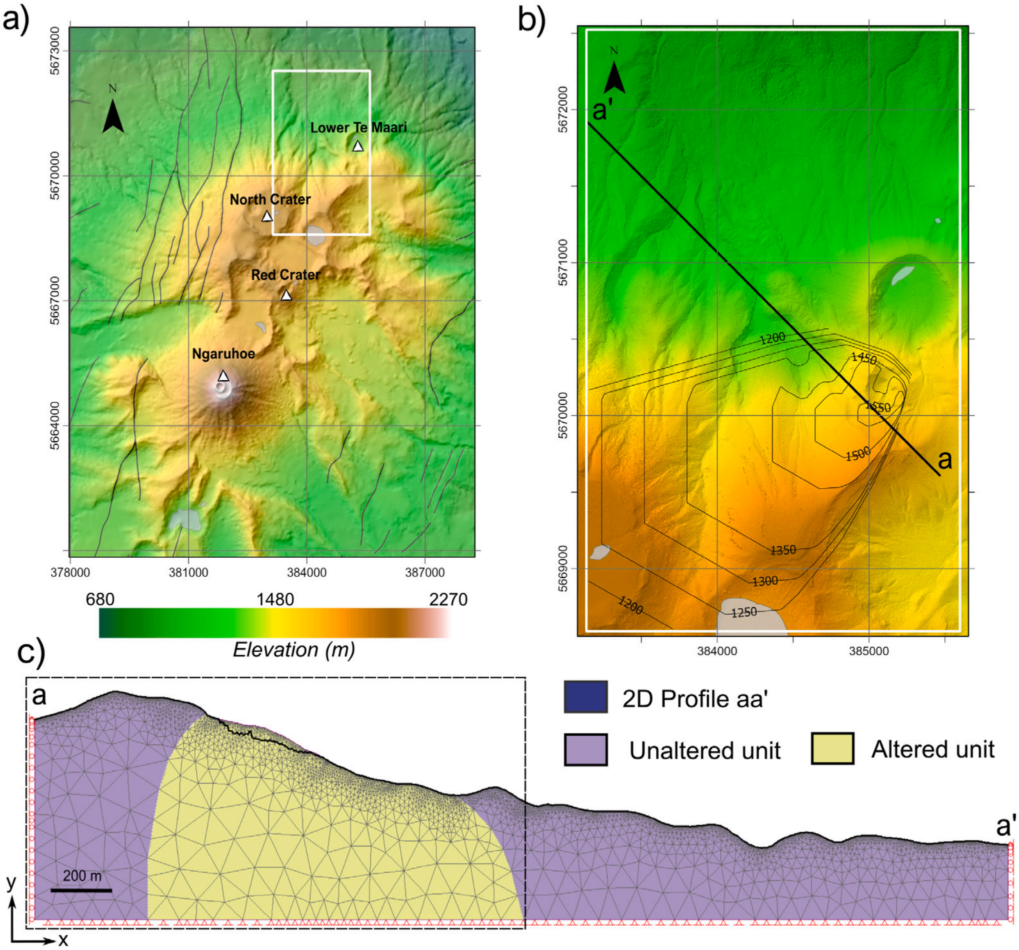

**Fig. 2.** (a) Topographic map of Tongariro. The white box highlights the area of interest. (b) Close-up of the area of interest, with contour lines representing the elevation (in metres) of the 3D volume modelled as the altered unit, created by merging the data from Kereszturi et al. (2018) and Miller and Williams-Jones (2016). (c) 2D model geometry along the aa' profile (black profile on subfigure b). Unaltered rocks are shown in purple, altered rocks in yellow. The grey mesh represents a 6-Nodded Triangles Graded Mesh. Red circles indicate restraints in the $x$-direction, red triangles represent restraints in all directions. The black line marks the post-topography of the observed source and the black dashed box outlines the area for results interpretation in subsequent figures.

mass. The GHB criterion defines material strength in terms of principal stresses as:

$$\sigma_1 = \sigma_3 + \sigma_{ci}(m_b\frac{\sigma_3}{\sigma_{ci}} + s)^a \qquad (1)$$

with $\sigma_1$ and $\sigma_3$, the respective major and minor principal stresses; $m_b$, $s$ and $a$, the empirical rock mass constants of the criterion; and $\sigma_{ci}$ the unconfined compressive strength (also referred as UCS).

When applying the GHB criterion, SSR-FEM returns the following reduced shear strength envelope (Hammah et al., 2005) at failure:

$$\tau_f = \frac{\tau}{SRF} = (\sigma_1 - \sigma_3)\frac{\sqrt{1 + am_b(m_b\frac{\sigma_3}{\sigma_{ci}} + s)^{a-1}}}{2 + am_b(m_b\frac{\sigma_3}{\sigma_{ci}} + s)^{a-1}} \cdot \frac{1}{SRF} \qquad (2)$$

$\tau$ represents the initial shear strength of the material. The reduced shear strength, denoted $\tau_f$, corresponds to the strength at which the model fails to converge, indicating the onset of failure in the rock mass. The Strength Reduction Factor, denoted as SRF, is the scalar factor applied to incrementally reduce the material strength in SSR-FEM approach, until the system becomes unstable. A SRF $\leq 1$ indicates that the slope is unstable in its modelled form.

Models based on the GHB criterion require the following essential numerical parameters:

- Young's modulus ($E$), quantifies the material's capacity to deform under the effect of an applied load.
- Poisson's ratio ($\nu$), characterises the relationship between transverse and longitudinal strains of the material when subjected to an applied load, giving a crucial information on how the material deforms.
- Unconfined Compressive Strength (UCS or $\sigma_{ci}$), corresponds to the highest stress that a rock can withstand when subjected to a unidirectional stress $\sigma_1$, without any lateral support. UCS, based on intact rock properties, serves as a reference strength in the GHB criterion.
- Geological Strength Index (GSI), is a visual index used for calculating the Hoek–Brown empirical constants ($m_b$, $s$ and $a$) (Hoek, 1994; Hoek and Brown, 1997; Hoek, 2005), and providing qualitative analyses of the surface conditions and structure of the rock mass (Marinos and Hoek, 2000).
- $m_i$, $m_b$ and $s$, are the Hoek–Brown empirical rock mass constants (Hoek and Brown, 1980). The disturbance factor D (Hoek et al., 2002), reflecting the impact of anthropogenic actions is fixed to 0.

The geomechanical properties (porosity, UCS, Young's modulus and Poisson's ratio) were estimated for the Te Maari edifice through multiple field surveys (Fig. 3) and a literature-based dataset (Table 1) of rock strength based on altered and unaltered andesitic rocks from Tongariro [Kidd et al. unpublished data] and analogous rocks from Ruapehu (Mordensky et al., 2018b; Schaefer et al., 2023) and Whakaari (Heap et al., 2015). The chosen analogue volcanic rocks are mineralogically similar

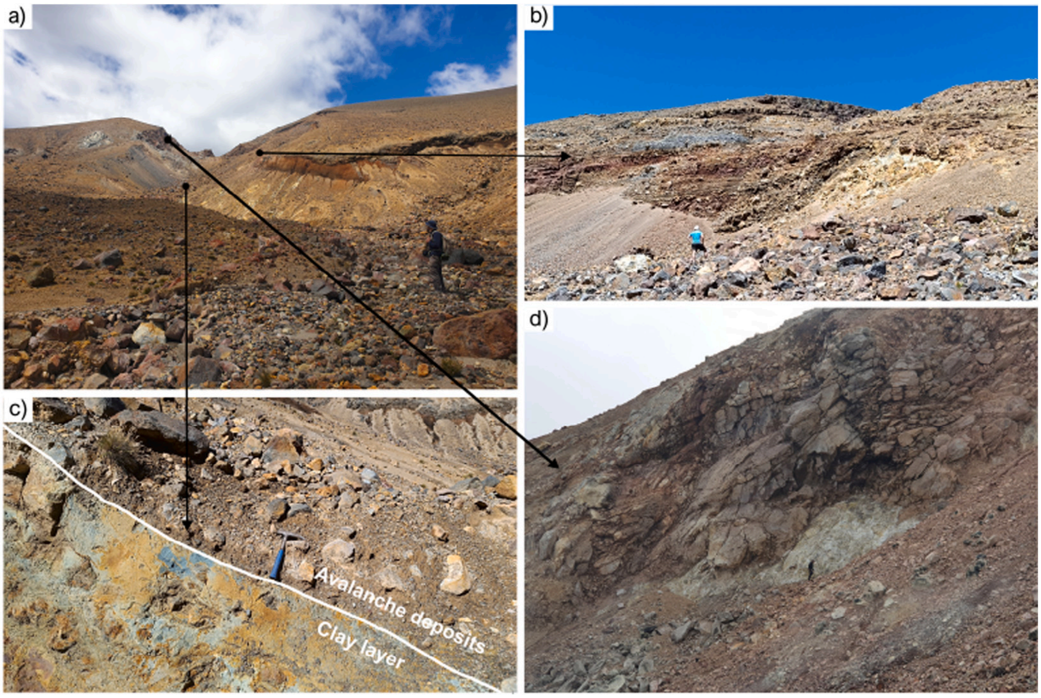

**Fig. 3.** Field photographs. (a) Down view of the channel and the scar from the 2012 Te Maari debris avalanche. (b) Altered pyroclastic deposits exposed on the western side of the debris avalanche scar. (c) Clay-rich layer (suspected to be the sliding surface) with debris avalanche deposits on top. (d) Altered lava flow on the eastern side of the debris avalanche scar. The black arrows show the approximate locations of photographs b, c and d on photograph a.

**Table 1**
Summary of the dataset used to determine the mechanical parameters of the altered and unaltered units.

| Unit | References (Number of samples) | Parameters | Lithology description |
|---|---|---|---|
| Altered Unit | Heap et al. (2015) (17) | UCS, $\phi$ | Hydrothermally altered ash tuff (Whaakari) |
| | Mordensky et al. (2018b) (33) | UCS, $\phi$, $E$, $v$ | Altered brecciated margin lava (Ruapehu) |
| | Schaefer et al. (2023) (4) | UCS, $\phi$, $E$ | Autoclastic breccia showing surface weathering (Ruapehu) |
| | Kidd et al, unpublished data (29) | UCS, $\phi$ | Lava showing intermediate argillic alteration (Tongariro) |
| Unaltered Unit | Mordensky et al. (2018b) (47) | UCS, $\phi$, $E$, $v$ | Unaltered dense coherent lava and unaltered intrusions (Ruapehu) |
| | Schaefer et al. (2023) (2) | UCS, $\phi$, $E$ | Unaltered lava (Ruapehu) |
| | Kidd et al, unpublished data (4) | UCS, $\phi$ | Unaltered lava (Ruapehu) |

(both fresh and altered samples) and are assumed to have similar mechanical properties.

To understand the effect of slope mechanical properties, we run simulations with three different material property configurations (Table 2): (1) a homogeneous slope (configuration H), where the entire slope consists of a single rock unit, tested in both a medium-strength unaltered unit (Ha) and a medium-strength altered unit (Hb); (2) a heterogeneous slope (configuration M) with two rock units — one altered and one unaltered — both with medium strength; and (3) a heterogeneous slope (configuration W) where the altered unit has low strength, while the unaltered unit maintains medium strength. The strength of the unaltered unit (i.e. UCS) is considered as the median from the collected dataset of unaltered rocks (Table 2). The UCS of the altered unit is estimated either from the median (configuration M) or the lower quartile (configuration W) of the collected dataset of altered rocks (Table 2). Accounting for these various mechanical configurations allows us to examine the effect of material strength on edifice stability.

The strength dataset (Table 1) is based on laboratory tests of intact rocks, and tends to overestimate the strength of the material. Therefore, field studies were undertaken to characterise the macroscopic-scale conditions of the rock masses involved in the collapse through the determination of the GSI. The GSI compares the strength of the rock mass with the laboratory-calculated strength of the intact rock, operating under the assumptions that the strength of the rock mass is controlled by its structure and joints, and that the intact rock samples are homogeneous without discontinuities (Hoek and Brown, 1997). Ranging from 0 to 100, the index represents a proportion of the laboratory-calculated stress. A lower GSI suggests that the total compressive force of the rock mass is a smaller fraction of the laboratory-calculated compressive force.

Field studies at Te Maari revealed that the debris avalanche deposits lie on a highly altered, clay-rich surface (Fig. 3c), which is suspected to be the sliding surface of the 2012 debris avalanche. This highly deformable layer supports our choice to use the FEM, which accounts

**Table 2**

Summary of the input parameters for each mechanical property configuration. Except for the weak-strength altered unit UCS (in configuration W), which is a lower quartile, all parameters are median values derived from a literature-based dataset made of 53 samples for the unaltered unit and 83 samples for the altered unit (Table 1).

| Slope configuration | Number of units | Unit properties | Unit strength (UCS) | Initial Conditions | Stiffness | | Strength | | | | Hydraulics |
|---|---|---|---|---|---|---|---|---|---|---|---|
| | | | | Unit weight (kN/m$^3$) | Poisson's ratio | Young's modulus (GPa) | UCS (MPa) | GSI | $m_B$ | $s$ | Porosity |
| Ha | 1 | Unaltered | Medium | 26 | 0.25 | 35 | 160 | 60 | 6.66 | 0.012 | 0.03 |
| Hb | 1 | Altered | Medium | 18 | 0.2 | 12 | 25 | 25 | 1.15 | 0.002 | 0.2 |
| M | 2 | Unaltered | Medium | 26 | 0.25 | 35 | 160 | 60 | 6.66 | 0.012 | 0.03 |
| | | Altered | Medium | 18 | 0.2 | 12 | 25 | 25 | 1.15 | 0.002 | 0.2 |
| W | 2 | Unaltered | Medium | 26 | 0.25 | 35 | 160 | 60 | 6.66 | 0.012 | 0.03 |
| | | Altered | Weak | 18 | 0.2 | 12 | 5 | 25 | 1.15 | 0.002 | 0.2 |

for the plasticity of the materials. Field studies also revealed that rock masses outcropping in the 2012 debris avalanche scar have different lithologies:

- The western side of the scar, which is composed of succession of loose pyroclastic deposits, rich in highly porous scoriaceous deposits, can be assimilated to the altered unit (Fig. 3b). It is the closest approximation of the material that formed the failed mass, described by Procter et al. (2014) as mainly composed of 'variably hydrothermally altered breccias, scoria, tuff and other coarse-grained diamictons'. This unit shows a disturbed to disintegrated structure with poorly interlocked mixture of angular to subrounded rock pieces, and poor surface conditions showing high level of alteration (sulfur stains, silica filling cracks). Regarding these conditions, we attribute a GSI ranging from 20 to 30 to that unit, which is consistent with GSI values attributed to similar formations in other studies (e.g. Mordensky et al. 2018a).
- Rock masses constituting the unaltered unit, notably the lava flow forming the eastern part of the channel, show an imbricated and blocky structure made up of cubic blocks ranging from half a meter to a meter, separated by orthogonal fractures, and good surface conditions with slightly altered, iron-stained surfaces (Fig. 3d). Closer to the scar, this lava flow shows local pocket of alteration on the surface (e.g. white precipitation within the joints, sulfur deposition, etc.). We estimate for this unit a GSI ranging from 55 to 65, which is consistent with typical ranges of GSI values found in the literature for fractured lavas (Moon et al., 2005; Heap et al., 2019).

GSI and porosity values are then used to calculate the empirical constants $m_i$, $m_b$ and $s$ (through the Eberhardt (2012) equations), associated with the GHB criterion. The parameters used for each mechanical property configuration (Ha, Hb, M and W) are presented in Table 2.

### *3.3. Groundwater and seismic acceleration conditions*

Whether fed by magmatic or meteoric fluids, the fluid circulation strongly modifies pore pressure and causes strength changes in the edifice. The three months preceding the eruption show no significant increase in rainfall compared with the monthly average over the last 30 years. Based on data from the two nearest NIWA stations recording over this period (Mt Ruapehu Chateau Ews and Tongariro Hatchery), we find that the quarterly average rainfall for May-August 2012 (266.9 mm and 189.2 mm respectively) is very similar to the quarterly average recorded for the same period between 1991 and 2020 (268.6 mm and 182.9 mm respectively). Therefore, the correlation between the circulation of rain water and instability is not demonstrated. Rainfall infiltration is therefore neglected in our simulations. However, the seismic record analysis suggests an injection of magmatic fluid prior to the event with small unlocatable micro-earthquakes at 23:46:50 (UTC +12), interpreted as increased flux of fluids from the shallow magma system (Jolly et al., 2014). This fluid injection could possibly have generated a rise in pore pressure throughout the hydrothermal system.

Accounting for this prior knowledge and the complexity of the hydrothermal system at Tongariro, we aim to better constrain the groundwater conditions beneath Te Maari, their effect on the pore pressure distribution, and the impact of these changes on slope stability. Hydrothermal activity and its effect on the stability at Te Maari is therefore modelled using assumptions of hydrostatic pore pressure changes and seepage (e.g. Mordensky et al. 2022). We tested the sensitivity of volcanic flank stability to different groundwater conditions and seismic effects with the following hydrostatic (configurations 1, 2 and 4), pseudo-static (configurations 3 and 5) and seepage (configurations 6 and 7) assumptions:

1. no groundwater.
2. a wet edifice with an increase in pore pressure using a higher pore pressure ratio in the altered unit (for heterogeneous material property configurations).
3. a wet edifice with an increase in pore pressure in the altered unit and seismic acceleration (pseudo-static coefficients based on acceleration data).
4. a wet edifice with a high perched water table due to the impermeable clay layer.
5. a wet edifice with a high perched water table due to the impermeable clay layer and seismic acceleration.
6. no infiltration.
7. a range of infiltration rates (from $1 \times 10^{-9}$ m s$^{-1}$ to $5 \times 10^{-6}$ m s$^{-1}$), travelling upward from depth due to hydrothermal fluid circulation.

Physical and mechanical boundary conditions allow movement at the top surface whereas movements are restrained in the horizontal direction for the lateral boundaries, and in all directions at the base surface (Fig. 2c). Pore pressure conditions for both hydrostatic and pseudo-static configurations were modelled as a single stage. Dynamic conditions for pseudo-static configurations are applied as pseudo-static loads to represent the earthquake ground motion during the event. For seepage configurations, a localised infiltration is applied at the base of the altered unit in a second model stage.

#### *3.3.1. Hydrostatic and pseudo-static models*

Configurations 2 and 3 assume an increase in pore pressure in the altered unit (Fig. 4a). In these cases, we establish a pore pressure ratio that evolves with depth as follows:

$$r_u = \frac{u}{\gamma z} \tag{3}$$

where $u$ is the pore-water pressure, $\gamma$ is the unit weight of the soil and $z$ is the depth below ground. Considering a saturated edifice, the unaltered unit is attributed to $r_u = 0.1$, and the altered unit to $r_u = 0.5$. This pore pressure ratio approximates hydrostatic pressure

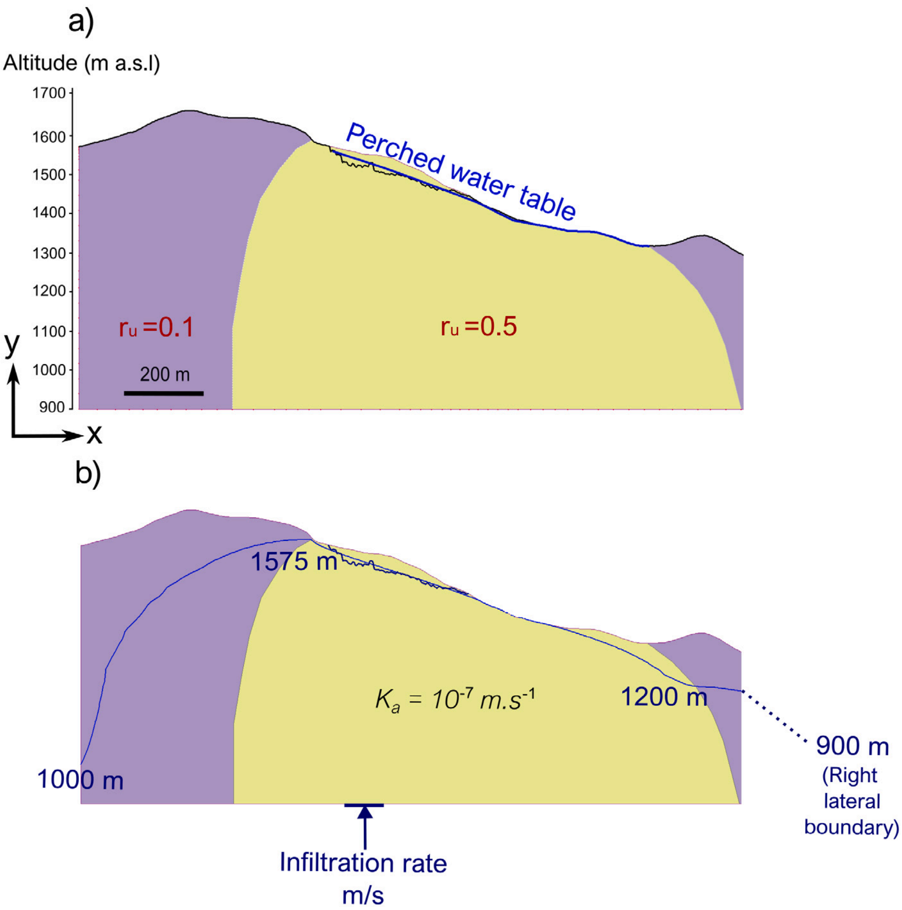

**Fig. 4.** Groundwater boundary conditions. (a) Hydrostatic assumptions. $R_u$ is the pore pressure ratio applied in each unit for configurations 2 and 3. Blue line represents the perched water table in configurations 4 and 5. (b) Seepage assumption. Blue line represents the total head (water table level). Depth of the total head (in meters) is indicated at each vertical boundary (both external and material). Upper external boundary is characterised by 0 flow or no groundwater. Lower boundary is characterised by infiltration. $K_a$ is the hydraulic conductivity of the altered unit.

in the altered unit and offers a reasonable, simplified and conservative estimate for saturated initial conditions (e.g. del Potro et al. 2013).

Configurations 4 and 5 assume the presence of the clay-rich sliding surface identified in field studies (Fig. 3c). This layer is likely the result of intermediate argillic alteration of an initially highly porous layer (e.g. pyroclastic deposits, Ball et al. 2018), leading to the precipitation of phyllosilicates, significantly reducing its permeability and forming local saturated zones (Ball et al., 2018). When these impermeable layers perch on the slopes of the edifice, shallow pore pressure can increase, thereby promoting instability (Ball et al., 2018). Building our hypothesis on the potential of this clay-rich layer to act as a local impermeable barrier to groundwater flow, we simulate a perched water table elevated at the top of this layer (Fig. 4a).

Analysis of the eruptive sequence of the 2012 event by Jolly et al. 2014 identifies an earthquake of magnitude 1.8, located within the head wall of the debris avalanche (Fig. 1). The latter is associated with the onset of the debris avalanche, but its trigger role has not been demonstrated. Given the small magnitude of this specific event, we do not consider it sufficient to independently explain the destabilisation. However, previous studies have demonstrated that the combined effect of rising pore pressure and low-magnitude earthquakes can destabilise volcanic edifices (e.g. Van Duong et al. 2023). In that sense, we assess its potential influence in conjunction with pore pressure rise in configurations 3 and 5. The pseudo-static method was used to simulate seismic acceleration, employing dimensionless seismic coefficients derived from the study of Peak Ground Acceleration (PGA). The PGA values of 0.003 g east, 0.005 g north, and 0.0013 g vertical were calculated from velocity data recorded at the TON2 station (Fig. 1). Given that the station is very close to the hypocentre (≈ 350 m) and assuming that local conditions are not significantly affected by amplification or strong attenuation, we based the calculation of the pseudo static seismic coefficients on these PGA values. Using Hynes-Griffin and Franklin (1984) method, an horizontal seismic coefficient of 0.020 (average of the x- an $y$-directions) and a vertical seismic coefficient of 0.0065 were vectorially added to the gravity force on each element of the mesh.

### 3.3.2. Seepage models

The hydrostatic pore pressure ratio approach (configurations 2 and 3) provides a useful preliminary assessment of slope stability without requiring detailed groundwater data. However, it can be considered more conservative (Mordensky et al., 2022) since it assumes that the edifice is completely saturated. On the other hand, the perched water table assumption (configurations 4 and 5) accounts for a partially saturated altered unit and unsaturated unaltered unit, which is still a simplified assumption.

A second set of models (configurations 6 and 7), also based on profile aa' (Fig. 2), are conducted to simulate the seepage effects, providing a more accurate assessment of the dynamic effects of pore pressure distribution on slope stability. This approach better represents rock heterogeneities by simulating groundwater level as a function of topography and accounting for the different hydraulic parameters of rock units (Mordensky et al., 2022). The rock mass hydraulic parameters were derived from Mordensky et al. (2022) based on the Pinnacle Ridge units at Ruapehu. We assigned a hydraulic conductivity, $K_a$ of $1 \times 10^{-7}$ m s$^{-1}$ to the altered unit and $K_u$ of $6 \times 10^{-7}$ m s$^{-1}$ to the unaltered unit. Investigations of the groundwater system at Te Maari indicate the presence of a gravitationally stable condensate layer at 1000 m a.s.l (Walsh et al., 1998; Hill et al., 2015; Miller et al., 2018), which serves as a base to fix the lateral hydraulic boundary conditions of the model with a total head fixed at 1000 m a.s.l on the left boundary and at 900 m a.s.l on the right boundary, representing the inclination of the water table (Fig. 4b). The seepage models assume an almost completely saturated altered unit with a total head fixed in the shallow layers.

Using the interpretation of the seismic record of the 2012 eruptive sequence by Jolly et al. (2014), we simulate a potential fluid infiltration by implementing a vertical infiltration rate at the base of the altered unit (Fig. 4b). The objectives, using seepage models, are to determine the impact of a vertical infiltration on pore pressure distribution and to identify the infiltration rates capable of replicating the 2012 failure.

In the following sections, we refer to our fourteen stability models using abbreviations that indicate both material properties and groundwater configurations (see Table 3). “H” represents homogeneous material, “M” indicates a medium-strength altered unit, and “W” stands for a weak-strength altered unit. Groundwater conditions are denoted by the corresponding number from the groundwater conditions list. For example, simulation M3 refers to a medium-strength altered unit under a pore pressure ratio ($r_u$) of 0.5.

## 4. Results

A total of 14 FEA simulations exhibiting different material, groundwater and seismic conditions were performed (Table 3). The stability of each simulation was quantified by calculating the critical SRF through the SSR method (Zienkiewicz et al., 1975), presented for each simulation in Table 3. This is the ratio of the initial strength parameters to the reduced strength parameters at failure. A SRF $\leq$ 1 indicates that the initial strength state of the material is unstable, making the slope more likely to fail. In homogeneous, dry edifice conditions, the SRF is significantly greater than 1. Generally, weaker materials (“W” configurations) yield a lower SRF, and higher pore pressures further reduce SRF values. Only two scenarios, simulations W3 and M7, result in SRF values below 1; both involve high pore pressure in the upper layers of the edifice.

In our study, we further investigate the potential zone of failure for each simulation using the maximum shear strain, which is defined as the largest angle of deformation within a material under an applied load and given as:

$$\gamma_{max} = \frac{\varepsilon_1 - \varepsilon_3}{2} \tag{4}$$

with $\gamma_{max}$, the maximum shear strain, $\varepsilon_1$ and $\varepsilon_3$, the minimum and maximum principal strain.

Shown as coincident with the slip surface by several laboratory tests (e.g. Roscoe 1970), maximum shear strain is simple to use, because of its hyperbolic dependency with the shear strength (Duncan and Chang, 1970; Matsui and San, 1992). Using this technique, the failure surface is not unique but consists in a yield zone extending from the base to the top of the slope (Matsui and San, 1992). This yield zone allows an interpretation of the overall location and geometry of the failure surface.

### 4.1. Effect of material properties and discontinuities on failure

The post-topography surface outline (Procter et al., 2014) is used to compare our results with the observed failure. Simulation results are presented as the maximum shear strain distribution (Fig. 5) corresponding to one or two strength-reduction stages past the critical SRF, which allows for a better visualisation of the failure propagation.

The mode and extent of failure in dry homogeneous (H1) conditions are approximately the same regardless of material properties, only affecting the critical SRF, which reduces from SRF = 9.17 (Table 3) for unaltered homogeneous (H1a) to SRF = 3.37 (Table 3) for altered homogenous configurations (H1b). Considering a dry, homogeneous edifice (H1) with unaltered (Fig. 5a and 5b) or altered material properties, strain is primarily concentrated in a graben-type extensional failure in the upper portion of the slope, with a deep-seated rotational failure toe (Fig. 5a). This progressively connects with the extensional failure at critical SRF to form a large rotational slip surface including the upper part of the slope (Fig. 5b). The strain concentration zone forms a slip surface of nearly 160 m deep and 930 m long (Fig. 5b) for both material property scenarios (H1a and H1b).

In comparison, M1 and W1, the dry heterogeneous configurations (Fig. 5c and 5d) show rotational strain concentration zones that are mainly confined to the altered unit. These zones do not extensively propagate into the upper portion of the slope, which is part of the unaltered unit (Fig. 5c and 5d). The disconnected extensional failure in the upper part of the slope is still observed. The resulting rotational failures are much narrower than the homogeneous simulations (H1), with collapse depths on average 50% smaller. Adding the altered unit also has a significant impact on the overall stability of the slope with a decrease in SRF (62%) for simulation M1 (Fig. 5c), which is more pronounced (78%) when the altered unit is weaker (simulation W1, Fig. 5d).

Therefore, considering an entirely homogeneous edifice (H1), the upper portion of the slope is always involved in a large deep-seated rotational failure. In contrast, a heterogeneous edifice (M1 and W1) results in localised rotational failures that more closely represent the slope failure at Te Maari. Despite showing shallower and thinner potential collapses, the dry heterogeneous simulations still overestimate the magnitude of collapse (i.e., the volume of material involved) and produce extensional failures in the upper portion of the slope. Moreover, these configurations exhibit SRF $\geq$ 2, indicating that the slope remain stable.

### 4.2. Effect of hydraulic properties on failure characteristics

Simulations using dry conditions (H1a, H1b, M1 and W1) cannot replicate the observed failure, thus other conditions (e.g. pore-water pressure) must be explored. Here, we explore the effect of groundwater parameters on stability to understand the impact of the hydrothermal system on the failure.

#### 4.2.1. Hydrostatic assumptions

Both the pore pressure ratio models (configurations 2 and 3) and the perched water table models (configurations 4 and 5) exhibit similar pore pressure profiles, closely approximating the hydrostatic pressure (Fig. 6). However, slight differences between these profiles are observed, particularly at shallower depths. In the pore pressure ratio models, the vertical pore pressure profile is slightly higher in the first 300 m compared to the perched water table configurations. The perched water table is approximately located at a depth of 30 metres, extending to the surface towards the northwestern boundary of the altered unit (Fig. 4a). Therefore, the pore pressure remains zero over the first 30 m in these models (Fig. 6), indicating an unsaturated layer without matrix suction effects.

Although the difference in pore pressure is small, it results in large variations in failure depths and extents (Fig. 7). In the perched water table models (Fig. 7c and 7d), the strain concentration zones reach maximum depths of approximately 110 m for simulation M4 and 130 m for simulation W4, both of which are significantly deeper than the observed failure depth. They also reveal a longer major axis, strongly controlled by the perched water table boundaries. Additionally, considering either weak (W4) or medium strength altered unit (M4), the initial slope conditions remain stable with a critical SRF $\geq$ 1. In contrast, the pore pressure ratio models (Fig. 7a and 7b) show strain concentration zones with substantially smaller maximum depths of approximately 55 m for simulation M2 and 65 m for simulation W2,

**Table 3**
Summary of the main conditions and results for each simulation. H and V stands respectively for horizontal and vertical pseudo-static seismic coefficients.

| | Conditions | | | | Results | |
|---|---|---|---|---|---|---|
| | Simulation | Groundwater configuration | Seismic coefficients (H ; V) | Material configuration | Critical SRF | Max Pore Pressure (MPa) |
| Hydrostatic & Pseudo-static | H1a | Dry | – | Unaltered homogeneous | 9.17 | NA |
| | H1b | Dry | – | Altered homogeneous | 3.37 | NA |
| | M1 | Dry | – | Medium unaltered (UU) and altered unit (AU) | 3.46 | NA |
| | W1 | Dry | – | Medium UU and weak AU | 2.02 | NA |
| | M2 | $R_u = 0.5$ | – | Medium UU and AU | 1.58 | 7.7 |
| | W2 | $R_u = 0.5$ | – | Medium UU and weak AU | **1** | 7.7 |
| | M3 | $R_u = 0.5$ | 0.020 ; 0.0065 | Medium UU and AU | 1.47 | 7.7 |
| | W3 | $R_u = 0.5$ | 0.020 ; 0.0065 | Medium UU and weak AU | **0.91** | 7.7 |
| | M4 | Perched water table | – | Medium UU and AU | 2.07 | 6.4 |
| | W4 | Perched water table | – | Medium UU and weak AU | 1.26 | 6.4 |
| | M5 | Perched water table | 0.020 ; 0.0065 | Medium UU and AU | 1.94 | 6.4 |
| | W5 | Perched water table | 0.020 ; 0.0065 | Medium UU and weak AU | 1.18 | 6.4 |
| Seepage | M6 | No infiltration | – | Medium UU and AU | 2.16 | 6.7 |
| | M7 | Infiltration rate: $1.5 \times 10^{-6}$ m $s^{-1}$ | – | Medium UU and AU | **0.97** | 8.7 |

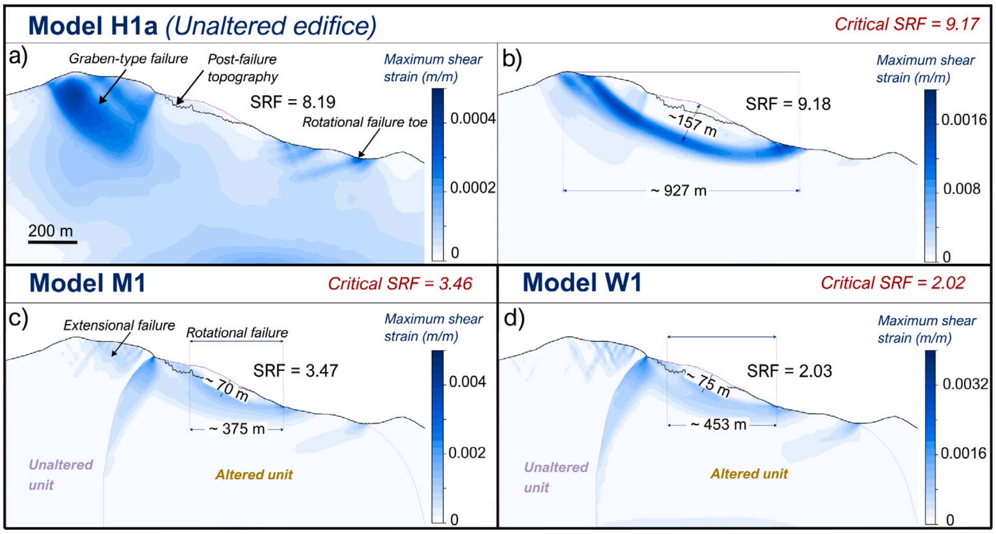

**Fig. 5.** Te Maari shear strain results under dry conditions. (a) Simulation H1a at multiple strength-reduction stages before the critical SRF and (b) at one strength-reduction stage beyond the critical SRF for a homogeneous unaltered edifice. (c) Simulation M1 at one stage beyond the critical SRF for a heterogeneous edifice. (d) Simulation W1 at one stage beyond the critical SRF for a heterogeneous edifice. The black line outlines the post-failure topography built from Procter et al. (2014) difference map.

as well as narrower extents. Simulation M2 presents a critical SRF of 1.58, whereas it reaches instability when considering a weak-strength altered unit (W2), with a critical SRF of 1. Despite a slightly deeper failure for simulation M2, both material property configurations show approximately the same failure geometry.

These results show that the pore pressure state of the upper layers significantly impacts the failure extent and depth. When the entire hydrothermal system is saturated and then subjected to high pore pressure (simulations M2 and W2), we observe shallower collapses, resulting in failure geometries similar to the observed failure. Therefore, we consider that the modelled pore pressure in these models is a reasonable simplified representation of the groundwater state during the event. The most notable difference between the observed and simulated result is the location of the failure, with the simulated failure shifted 80 m to the northwest. Instability conditions are also achieved with a SRF of 1 when considering a weak-strength altered unit (W2).

### 4.2.2. Seepage assumption

By testing a wide range of infiltration rates (from $1 \times 10^{-9}$ to $5 \times 10^{-6}$ m $s^{-1}$), we determined the vertical infiltration rates that could have triggered the observed failure depth. The infiltration point is located at an approximate depth of 600 m. To compare the data collected from each infiltration rate simulation, we compare results using pore pressure at a depth of 30 m, as this corresponds to the approximate depth of the observed failure surface above the infiltration point.

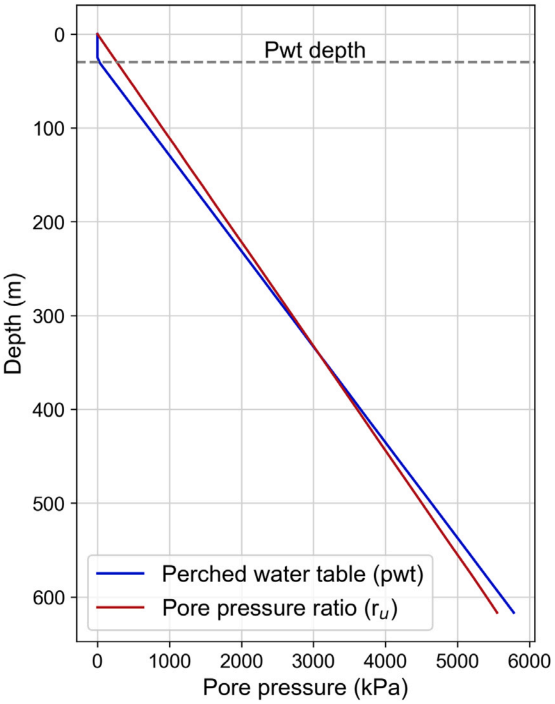

**Fig. 6.** Pore pressure profiles with depth along the black vertical profile shown in Fig. 7a, for both hydrostatic groundwater configurations: perched water table (blue) and pore pressure ratio (red).

The results of infiltration rate simulations (Fig. 8) show very large potential failure depths (70–100 m) and low pore pressures at failure depth (P30) when the infiltration rates are lower than the hydraulic conductivity ($1 \times 10^{-7}$ m $s^{-1}$). In contrast, the results show a linear increase in pore pressure (P30) and generally shallower failure depths (25–70 m) when infiltration rates are higher than the hydraulic conductivity. Collapses (SRF $\leq 1$) occur with infiltration rates of at least $10^{-6}$ m $s^{-1}$, corresponding to a pore pressure threshold of 200 kPa at failure depth. This infiltration rate corresponds to a maximum infiltration pressure of 8 MPa, which results in an excess pore pressure of $\approx 1.5$ MPa above hydrostatic at the infiltration site, indicating that even a relatively minor change in pore pressure is sufficient to promote instability.

We attribute the results in Fig. 8 to the development of a positive pore-pressure front due to infiltration at depth. As the infiltration rates exceed the hydraulic conductivity of the material, excess water rapidly accumulates due to limited drainage options. This leads to increased pore pressure around the infiltration point, which then progressively propagates throughout the system. The saturation front is then pushed through the initially unsaturated upper layers leading to a buildup of shallow pore pressure (Fig. 8). Building pore pressure in the shallow layers tends to promote shallower failures (Ball et al., 2018). Conversely, if the infiltration rates are lower than the hydraulic conductivity, the infiltrated fluid does not impact the upper layers where the pore pressure remains zero, and the rocks remain stable (Fig. 8).

Among the unstable infiltration scenarios (Fig. 8), the two modelled combinations of infiltration rates of $1.5 \times 10^{-6}$ m $s^{-1}$ (simulation M7, Fig. 9c), and $2 \times 10^{-6}$ m $s^{-1}$, corresponding to 30-meter depth pore pressures of respectively $\approx 260$ kPa and $\approx 290$ kPa, provide the most accurate representations of the observed failure depth and shape (Figs. 8 and 9c), despite a northward shift of approximately 150 m. In contrast, the no infiltration scenario (simulation M6, Fig. 9b), with a water table level approximately aligning with the sliding surface, exhibits a wide and deep failure, reaching a depth of 110 m, which closely resembles the results of the hydrostatic simulations M4 and W4 considering a perched water table (Fig. 7). Additionally, for simulation M7, considering an infiltration rate of $1.5 \times 10^{-6}$ m $s^{-1}$, we note the development of multiple shear bands, tilted in the slope direction, propagating from the slope surface to the main slip surface, indicating the potential for a retrogressive failure (Fig. 9).

### 4.3. *Effect of seismic ground acceleration on failure onset*

Our pseudo-static models allow us to evaluate the combined destabilising effects of the low-magnitude earthquake located within the head wall of the debris avalanche (Jolly et al., 2014) and the groundwater circulation.

Pseudo-static seismic loading reduces stability by approximately 6%–9% compared to simulations without seismic loading, which in most cases, is insufficient to trigger collapse. Models considering a perched water table indicate that instability (critical SRF $\leq 1$) is not reached with (simulations M5 and W5, Fig. 10) or without ground acceleration (simulations M4 and W4, Fig. 7). Similarly, models accounting for a pore pressure ratio and a medium-strength altered unit show no instability (critical SRF $> 1$) with (simulation M3, Fig. 10) or without ground acceleration (simulations M2, Fig. 7). The only scenario in which the earthquake acts as a trigger is simulation W3, which considers a pore pressure ratio and a weak-strength altered unit. However, simulation W2 (without seismic loading) already indicates a critically unstable initial state (critical SRF of 1).

Therefore, for seismic ground acceleration to act as a trigger, the slope must already be substantially weakened by other preparatory factors (e.g., alteration, pore pressure increase). Compared to seismic loading, the destabilising effect of groundwater is much greater. For example, groundwater parameters alone lead to an average 40% reduction in critical SRF compared to dry simulations (Figs. 5 and 7). Moreover, no significant changes in terms of failure geometry and magnitude are observed when adding the pseudo-static seismic coefficients.

## 5. Discussion

### 5.1. *Pre-event conditions: pore pressure-driven failure*

Volcanic debris avalanches evolve in stages and failure cannot be attributed to a single controlling factor, but is influenced by a combination of preparatory and triggering factors (Van Asch et al., 2007). Focusing on the pre-failure and failure stages, our Te Maari FEM results enable us to describe the complex interplay between these preparatory and triggering factors (inputs) and the slope responses (outputs) at various pre-event scenarios tested under simplified assumptions.

Unlike homogeneous cases, where failure extent and depth are largely governed by slope geometry and gradient (Zhang et al., 2013; Sharma, 2013), composite volcanoes with hydrothermally altered rock masses experience more complex failures, influenced by multiple factors. These volcanoes are built by layered eruptive products, including lavas, pyroclastic and lahar deposits, each with distinct initial strengths and alteration potentials (John et al., 2008; Mielke et al., 2015; Ball et al., 2018). Such material discontinuities are particularly conducive to instability, as they accumulate the highest deformation rates. Our results highlight that in hydrothermally-affected failures, the mechanical properties of the materials and their local geometry (e.g. layering, discontinuities) play a significant role in determining the probable failure extent. A simplified heterogeneous geometry (comprising an altered and unaltered unit) effectively captures the location of the failure surface in both area and depth.

Moreover, understanding hydrothermal fluid circulation is crucial, as it may induce thermomechanical fracturing and chemical alteration processes. It may also cause transient changes in pore pressure, a common trigger for shallow failures (Van Asch et al., 2007; Ball et al., 2018)

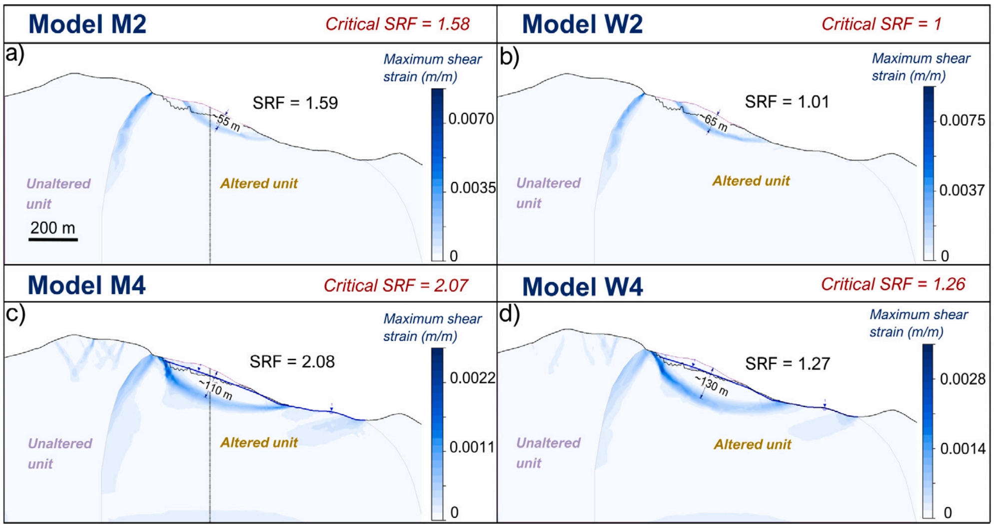

**Fig. 7.** Te Maari shear strain results under hydrostatic groundwater configurations. (a) Simulations M2 and (b) W2 at one strength-reduction stage beyond the critical SRF. (c) Simulations M4 and (d) W4 at one strength-reduction stage beyond the critical SRF.

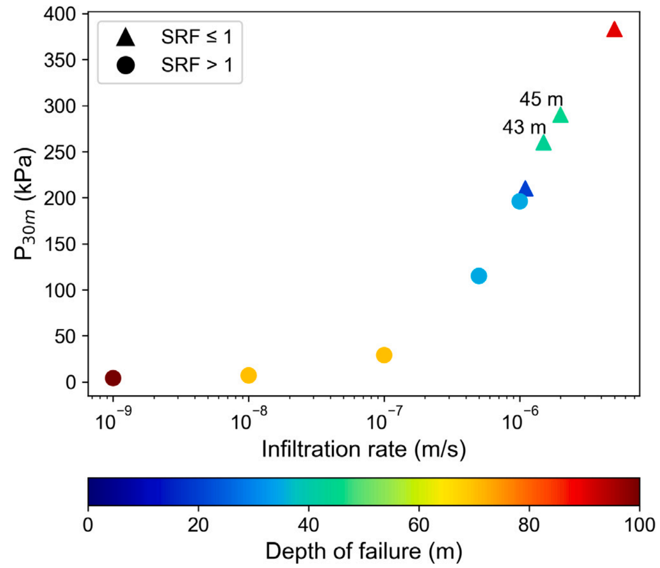

**Fig. 8.** Infiltration rate values (m $s^{-1}$) leading to instability (triangular markers, SRF≤1) and stability (circular markers, SRF>1) as a function of the pore pressure at 30 m depth. Colour scale displays the maximum depth of the modelled failure for each scenario.

within hydrothermal systems. By reducing effective stresses, material strength is lowered and the stability threshold can be overcome. Our simulations suggest that the 2012 failure was heavily influenced by the groundwater conditions within the edifice. Simulations neglecting pore pressure effects and focusing only on the mechanical properties of a dry edifice (H1a, H1b, M1 and W1, Fig. 5) result in significant overestimates of the stability and the volumes of potential collapses. The presence of water in the edifice reduces the SRF by 50%–60%, with significant changes in collapse volumes. Simulations incorporating positive pore pressures within the upper layers (simulations M2 and W2, Fig. 7; simulation M7, Fig. 9; simulations M3 and W3, Fig. 10) of the edifice were able to reproduce similar failure depths as the observed failure. Simulations considering a perched water table approximately 30 to 40 meters deep (simulations M4 and W4, Fig. 7; simulation M6, Fig. 9; simulations M5 and W5, Fig. 10) result in more substantial failures, as there is no pore pressure reducing the effective stresses in the upper layers. Elevated pore pressure in the shallow regions of the edifice results in shallower failures and smaller collapse volumes (Ball et al., 2018), indicating its role in the small localised failure at Te Maari in 2012.

Consequently, we attribute instability at Te Maari to two mechanisms: strength reduction due to rock alteration and elevated pore pressures at shallow depths. The relationship between these mechanisms is not clearly demonstrated by our simulations. However, our simulations show that simply considering the presence of an impermeable layer (potentially formed by clay precipitation) does not replicate the magnitude of the observed failure. An increase in pore pressure in the shallow layers is necessary to replicate the observed instability. Our simulations also indicate that the likely trigger for this pore pressure increase is fluid infiltration from depth within the hydrothermal system (simulation M7, Fig. 9c), supporting the seismic interpretation of Jolly et al. (2014). This configuration can reproduce failure depths and shapes similar to those observed but is less constrained than the hydrostatic model, which is better at locating the failure. Infiltration models carry more uncertainties, particularly regarding the location of the infiltration point, which significantly influences the failure's position. Nevertheless, the hydrostatic model, assuming a uniform pore pressure ratio to represent elevated pore pressures in the altered unit, fails to capture the heterogeneous permeability structures characteristic of a composite volcano slope (del Potro et al., 2013; Ball et al., 2018). Moreover, the interplay between rock mechanics and groundwater circulation is complex and other unexplored effects could contribute to instability (e.g. thermodynamic effects).

### 5.2. Failure mechanics over time

FEM enables an evaluation of displacements, stresses, and deformations across the entire edifice. This method proves particularly suitable for inferring progressive slope failure influenced by deformations and time.

Visual analysis of Te Maari's post-event topography using the LiDAR survey carried out in November 2012 by Procter et al. (2014) reveals a circular failure with a failure plane angle of ≈ 20°. A discontinuity in the failure plane is observed, which we interpret as the limit between two ellipsoidal failures (approximated on Fig. 11): slide block 1 (SB1), with its top part attributed to the discontinuity detected by LiDAR analysis and a failure plane angle of ≈ 23°; and slide block 2 (SB2), with its base attributed to the discontinuity location and a failure plane angle of ≈ 20°.

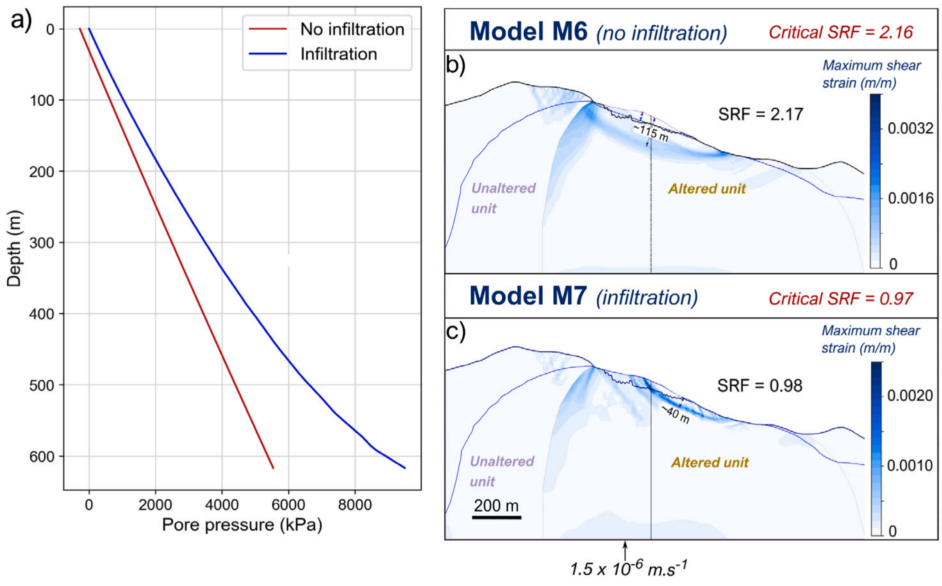

**Fig. 9.** (a) Pore pressure profiles along the black vertical query for simulation M6, without infiltration (red) and for simulation M7, with infiltration (blue). (b) and (c) are Te Maari shear strain results under seepage groundwater configurations: without infiltration (b) and with an infiltration of 1.5 × $10^{-6}$ m $s^{-1}$ (c).

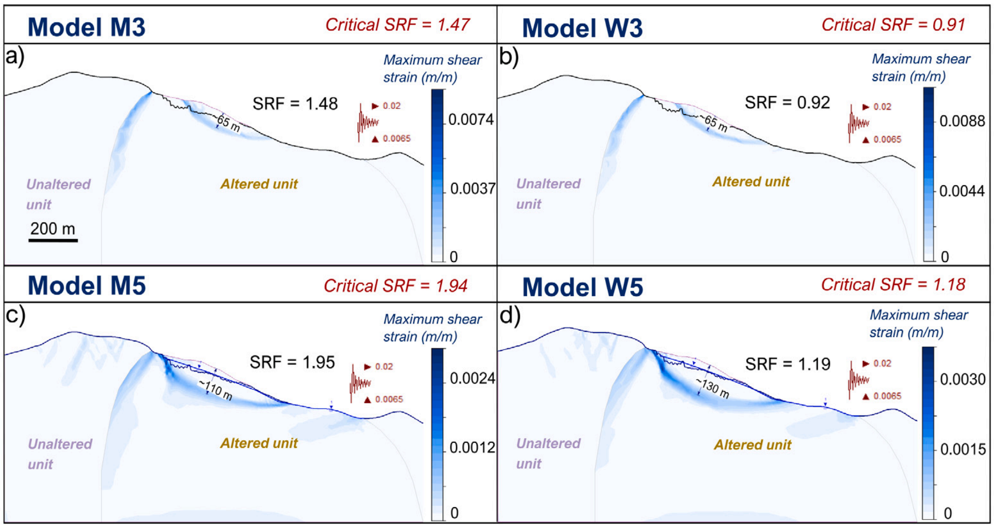

**Fig. 10.** Te Maari shear strain results under hydrostatic groundwater configurations and pseudo-static seismic loading. (a) Simulations M3 and (b) W3 under pore pressure ratio assumption + seismic loading. (c) Simulations M5 and (d) W5 under perched water table assumption + seismic loading.

The topography of this slip surface (Fig. 11) suggests a two-stage progressive failure, characterised by the collapse of SB1 followed by SB2. This hypothesis is supported by our simulations, which were based on the closest result to the initial phase location (SB1) of the collapse (Fig. 11). Therefore, we used simulation M2 (Fig. 7) to delineate SB1 outline (red outline in Fig. 12). Comparing this outline with the LiDAR visual analysis, we find that the modelled slip surface approximately aligns with the extent and position of the observed SB1 (Fig. 11). However, a slight northward shift (10 to 15 m) of the failure base is noted, potentially due to model uncertainties (e.g. pre-event DEM uncertainty) or residual material within the scar.

We propose that the second phase of the failure is characterised by the collapse of SB2 in response to the destabilisation of SB1. To test this hypothesis, a 2D simulation (Fig. 12), built with the M2 post-SB1 collapse topography as the external boundary and the same strength and pore pressure parameters, was performed. With a critical SRF <1, the material is unstable and therefore collapses. At the critical SRF, the extent of the simulated SB2, defined by the surface of maximum shear strain in Fig. 12b, is smaller than the SB2 observed by LiDAR analysis. However, examining several strength-reduction stages after the critical SRF (Fig. 12c) reveals that the failure propagation aligns with the observed slip surface of SB2 (Fig. 11).

Our 2D model (Fig. 12) then confirms that a second block collapses in response to the sliding of the first block. Confirming the progressive failure hypothesis through field measurements or satellite imagery can be challenging (Moretti et al., 2015). However, additional work can be carried out to determine the number and timing of each failure phase by analysing the forces inverted from the long-period seismograms (Favreau et al., 2010; Moretti et al., 2012, 2015; Mitchell et al., 2022).

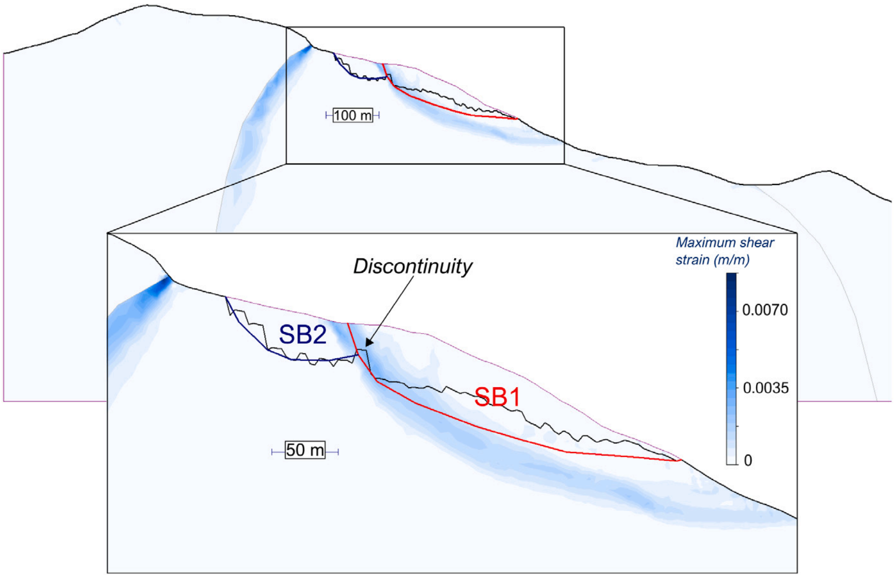

**Fig. 11.** Te Maari shear strain simulation M2 at critical SRF. Post-event topography (black line, Procter et al. 2014) overprinted on the 2D profile. Red line indicates the approximate slip surface of SB1 based on the post-event topography. Blue line delineates the approximate slip surface of SB2 based on the post-event topography.

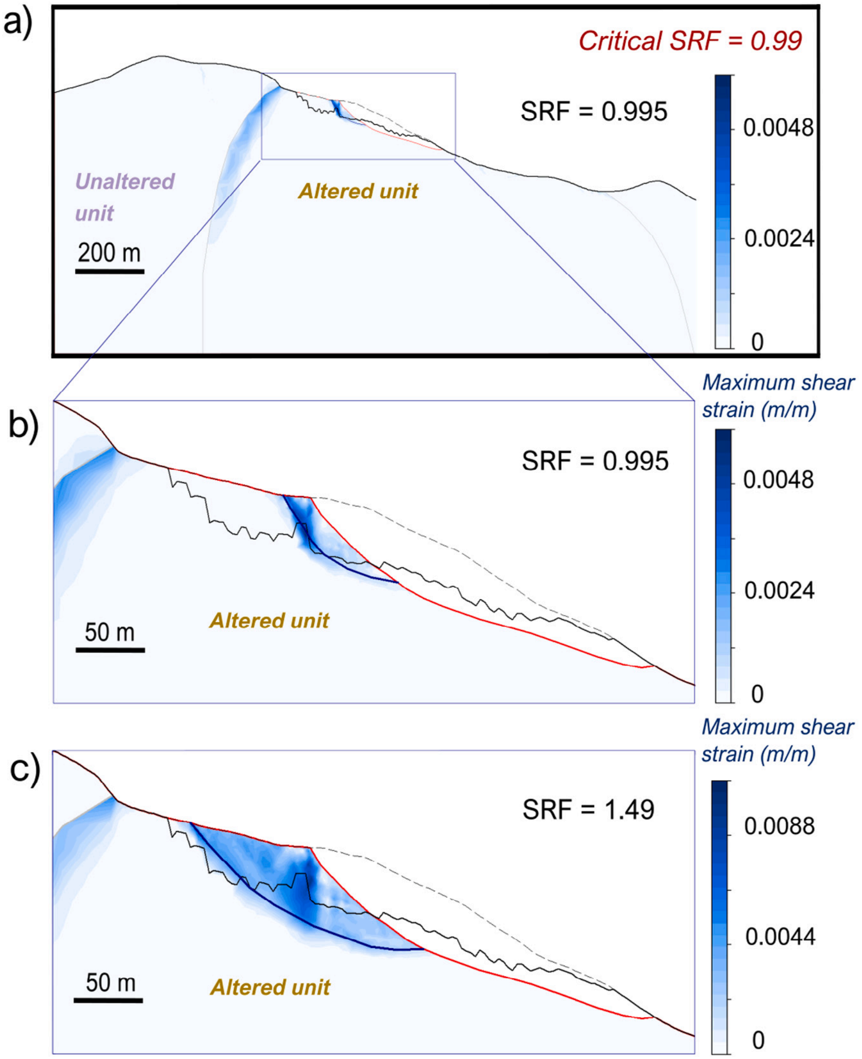

**Fig. 12.** Progressive failure model. (a) Te Maari shear strain simulation at critical SRF, on post-event topography from simulation M2. (b) Zoom on failure location at critical SRF (c) Zoom on failure location at SRF = 1.49. Black dashed outline represents the pre-event topography. Red line delineates the modelled post-topography after the collapse of SB1. Blue line delineates the modelled post-topography after the collapse of SB2.

### *5.3. Implication for future hazard assessment*

Consistent with previous studies (e.g. Finn et al. 2018, Ball et al. 2018, Mordensky et al. 2022), our simulations highlight the influence of various parameters, especially alteration and groundwater parameters, on volcanic flank stability. Our results show that the presence of water-saturated altered rocks within the edifice significantly decreases the SRF with associated changes in collapse volumes. An increase in pore pressure in the shallow part of the edifice (e.g. through an elevated water table) tends to trigger shallow and minor collapses, as demonstrated by Ball et al. (2018). Seepage analysis results for Te Maari have shown that even a relatively deep infiltration can induce fluctuations in water-table elevations, thus modifying the pore pressure in the shallow layers of the edifice.

The outcomes of our simulations are primarily influenced by the accuracy of the hydrological parameters rather than the geomechanical parameters (Okunishi and Okimura, 1987; Haneberg, 1991; Van Asch et al., 2007). Simulations that do not consider the fluid distribution within the edifice generally result in an overestimation of slope stability and potential collapse volumes compared to the Te Maari failure. However, the accuracy of our hydrological configurations are limited by the relatively low-resolution groundwater data. Therefore, to refine the three-dimensional distribution of pervasive alteration and shallow groundwater within New Zealand's volcanoes, more detailed geophysical surveys must be conducted, e.g. involving detection by electromagnetic data or induced polarisation (Finn et al., 2001, 2007; Miller and Williams-Jones, 2016; Revil et al., 2017; Finn et al., 2018). Low electrical resistivities characterise zones of hydrothermally altered volcanic rocks (due to their water and clay content) as well as groundwater of various salinities (Finizola et al., 2006; Finn et al., 2007). In addition to these geophysical analyses, regular monitoring of springs or wells located around the edifices can serve as a quick and cost-effective initial step in assessing the stability of active volcanoes (Ball et al., 2018).

Post-eruption field investigations and airborne hyperspectral imaging (Kereszturi et al., 2018) indicate that additional areas can substantially be affected by hydrothermal alteration, especially around Red Crater, Ketetahi Hot Springs and Te Maari craters (Fig. 1). Our simulations show that considering an altered material strongly decreases edifice stability, primarily due to the weakening of rock strength caused by chemical replacement of primary minerals. Therefore, by considering hydrothermal alteration as first-order potential sources of debris flow, a scenario similar to the 2012 event may be repeated, and can pose a significant danger, especially to both infrastructures and hikers on the Tongariro Alpine Crossing.

## 6. Conclusions

The interaction between preparatory and triggering factors offers insight into the complex mechanics underlying the 2012 debris avalanche at Te Maari. Our simulations highlighted several aspects of this complexity.

Firstly, the magnitude and shape of the collapse are primarily controlled by the heterogeneous nature of the edifice and the circulation of hydrothermal fluids. Simulations indicating relatively minor ($\approx$ 250 kPa) change in pore pressure in the upper layers were able to replicate instabilities with geometries and magnitudes closely similar to the observed failure, confirming the failure was driven by a pore pressure change. This mechanism also accounts for its shallow depth (Ball et al., 2018), illustrating the significant potential impact of slight pore pressure variations on stability. The triggering effect of the small-magnitude earthquake, identified by Jolly et al. (2014), is only demonstrated for a specific set of parameters, which necessarily involves an increase in pore pressure in shallow layers and the presence of weak-strength altered materials. This set of parameters tends to underestimate material strength, suggesting that the earthquake may just be a consequence of the groundwater circulation or the debris avalanche itself.

Secondly, our analysis of the observed post-failure topography reveals two ellipsoidal scars. Additional simulations on post-event topography suggested that the 2012 failure at Te Maari was progressive. Highlighting the dynamics of the failure at Te Maari, these simulations indicate a two-stage failure where the destabilisation of a first block led to the subsequent failure of the second block. The progressive nature of this failure would affect flow dynamics, increasing the complexity of the flow. Depending on the time interval between collapses, it can either cause deceleration, when phases act independently and material deposition obstructs the flow path, or acceleration, when phases act dependently, increasing momentum.

Thirdly, in terms of hazard assessment, the post-failure phase presents the main risk to nearby populations and infrastructures. Therefore, debris avalanche risk assessment requires a comprehensive understanding of flow dynamics, by the quantification of flow physical parameters such as runout distances, movement velocities, and inundation depths. These properties are largely influenced by the conditions at failure (preparatory and triggering factors). Our study shows that it is essential to better constrain these conditions, particularly the extent of the hydrothermal system and the groundwater distribution within the edifice, as it can significantly reduce stability and affect the magnitude and sequence of collapse. Additionally, the presence of water in the failed mass can affect the flow dynamics by causing fluidisation, thereby increasing the runout distance and potential impact area. On Te Maari, but also on other New Zealand stratovolcanoes (e.g. Ruapehu, Whakaari), significant areas of hydrothermally altered rock remain (Kereszturi et al., 2018, 2021) contributing to reduced stability. Consequently, a scenario similar to the 2012 event may be repeated, posing a significant risk to both infrastructures and population in New Zealand.

## CRediT authorship contribution statement

**Juliette Vicente:** Writing – original draft, Validation, Software, Methodology, Investigation, Formal analysis, Data curation, Conceptualization. **Stuart Mead:** Writing – review & editing, Validation, Supervision, Resources, Methodology, Investigation, Conceptualization. **Gabor Kereszturi:** Writing – review & editing, Supervision, Resources, Investigation. **Craig Miller:** Writing – review & editing, Resources, Funding acquisition.

## Declaration of competing interest

The authors declare that they have no known competing financial interests or personal relationships that could have appeared to influence the work reported in this paper.

## Acknowledgements

The authors are funded by the Beneath the Waves programme (Grant C05X2102) financed by the New Zealand Ministry of Business, Innovation and Employment (MBIE), with additional financial support from Project Tongariro for Juliette Vicente. Thanks to Maia Kidd for her unpublished mechanical property data on Tongariro, and thanks to Brian Perttu for the 1 m DEM used in Figs. 1 and 2. We also thank Lucia Capra and an anonymous reviewer for their valuable comments, that helped strengthened the manuscript.

## Data availability

Data will be made available on request.

## References

Ball, J.L., Taron, J., Hurwitz, S., Reid, M.E., 2015. Pore pressure distribution and flank instability in hydrothermally altered stratovolcanoes. In: AGU Fall Meeting Abstracts, vol. 2015. pp. V31F–03.

Ball, J., Taron, J., Reid, M., Hurwitz, S., Finn, C., Bedrosian, P., 2018. Combining multiphase groundwater flow and slope stability models to assess stratovolcano flank collapse in the Cascade Range. J. Geophys. Res.: Solid Earth 123, 2787–2805.

Belousov, A., 1996. Deposits of the 30 march 1956 directed blast at Bezymianny volcano, Kamchatka, Russia. Bull. Volcanol. 57, 649–662.

Belousov, A., Voight, B., Belousova, M., 2007. Directed blasts and blast-generated pyroclastic density currents: a comparison of the Bezymianny 1956, Mount St Helens 1980, and Soufrière Hills, Montserrat 1997 eruptions and deposits. Bull. Volcanol. 69, 701–740.

Bouligand, C., Coutant, O., Glen, J.M., 2016. Sub-surface structure of La Soufrière of Guadeloupe lava dome deduced from a ground-based magnetic survey. J. Volcanol. Geotherm. Res. 321, 171–181.

Brown, E.T., 1970. Strength of models of rock with intermittent joints. J. the Soil Mech. Found. Div. 96, 1935–1949.

Calder, E., Luckett, R., Sparks, R., Voight, B., 2002. Mechanisms of lava dome instability and generation of rockfalls and pyroclastic flows at Soufriere Hills Volcano, Montserrat. Geol. Soc. Lond. Memoirs 21, 173–190.

Carn, S., Watts, R., Thompson, G., Norton, G., 2004. Anatomy of a lava dome collapse: the 20 March 2000 event at Soufrière Hills Volcano, Montserrat. J. Volcanol. Geotherm. Res. 131, 241–264.

Cecchi, E., van Wyk de Vries, B., Lavest, J.-M., 2004. Flank spreading and collapse of weak-cored volcanoes. Bull. Volcanol. 67, 72–91.

Chang, Y., Huang, T., 2005. Slope stability analysis using strength reduction technique. J. Chin. Inst. Eng. 28, 231–240.

Christenson, B., Britten, K., Mazot, A., Fitzgerald, J., 2013. The 2012 Eruption of Te Maari, New Zealand: Characteristics of a shallow magmatic degassing event. In: AGU Fall Meeting Abstracts, vol. 2013. V24C–05.

Clarke, J., Adam, L., van Wijk, K., 2021. LP or VT signals? How intrinsic attenuation influences volcano seismic signatures constrained by Whakaari volcano parameters. J. Volcanol. Geotherm. Res. 418, 107337.

Cole, R., White, J., Conway, C., Leonard, G., Townsend, D., Pure, L., 2018. The glaciovolcanic evolution of an andesitic edifice, South Crater, Tongariro volcano, New Zealand. J. Volcanol. Geotherm. Res. 352, 55–77.

Cronin, S.J., Neall, V., Palmer, A., 1997. Lahar history and hazard of the Tongariro River, northeastern Tongariro Volcanic Centre, New Zealand. N. Z. J. Geol. Geophys. 40, 383–393.

Crouch, J.F., Pardo, N., Miller, C.A., 2014. Dual polarisation C-band weather radar imagery of the 6 August 2012 Te Maari eruption, Mount Tongariro, New Zealand. J. Volcanol. Geotherm. Res. 286, 415–436.

Crozier, M., 1986. Landslides: Causes, Consequences & Environment, vol. 252. Croom Helm London.

Dawson, E., Roth, W., Drescher, A., 1999. Slope stability analysis by strength reduction. Geotechnique 49, 835–840.

De Moor, J., Stix, J., Avard, G., Muller, C., Corrales, E., Diaz, J., Alan, A., Brenes, J., Pacheco, J., Aiuppa, A., 2019. Insights on hydrothermal-magmatic interactions and eruptive processes at Poás Volcano (Costa Rica) from high-frequency gas monitoring and drone measurements. Geophys. Res. Lett. 46, 1293–1302.

Duncan, J., 1996. State of the art: limit equilibrium and finite-element analysis of slopes. J. Geotech. Eng. 122, 577–596.

Duncan, J., Chang, C., 1970. Nonlinear analysis of stress and strain in soils. J. the Soil Mech. Found. Div. 96, 1629–1653.

Duncan, J.M., Wright, S.G., Brandon, T.L., 2014. Soil Strength and Slope Stability. John Wiley & Sons.

Eaves, S.R., Brook, M.S., 2021. Glaciers and glaciation of North Island, New Zealand. N. Z. J. Geol. Geophys. 64, 1–20.

Eberhardt, E., 2012. The Hoek-Brown failure criterion. Rock Mech. Rock Eng. 45, 981–988.

Favreau, P., Mangeney, A., Lucas, A., Crosta, G., Bouchut, F., 2010. Numerical modeling of landquakes. Geophys. Res. Lett. 37.

Finizola, A., Revil, A., Rizzo, E., Piscitelli, S., Ricci, T., Morin, J., Angeletti, B., Mocochain, L., Sortino, F., 2006. Hydrogeological insights at Stromboli volcano (Italy) from geoelectrical, temperature, and $CO_2$ soil degassing investigations. Geophys. Res. Lett. 33.

Finn, C.A., Deszcz-Pan, M., Anderson, E.D., John, D.A., 2007. Three-dimensional geophysical mapping of rock alteration and water content at Mount Adams, Washington: Implications for lahar hazards. J. Geophys. Res.: Solid Earth 112.

Finn, C., Deszcz-Pan, M., Ball, J., Bloss, B., Minsley, B., 2018. Three-dimensional geophysical mapping of shallow water saturated altered rocks at Mount Baker, Washington: Implications for slope stability. J. Volcanol. Geotherm. Res. 357, 261–275.

Finn, C.A., Sisson, T.W., Deszcz-Pan, M., 2001. Aerogeophysical measurements reveal collapseprone hydrothermally altered zones at Mount Rainier Volcano, Washington. In: 14th EEGS Symposium on the Application of Geophysics To Engineering and Environmental Problems. European Association of Geoscientists & Engineers, pp. cp–192.

Flageollet, J., 1996. The time dimension in the study of mass movements. Geomorphology 15, 185–190.

Glicken, H., 1996. Rockslide-Debris Avalanche of May 18, 1980, Mount St. Helens Volcano, Washington. US Geological Survey, Cascades Volcano Observatory.

Hammah, R., Yacoub, T., Corkum, B., Curran, J., 2005. The shear strength reduction method for the generalized Hoek-Brown criterion. In: ARMA US Rock Mechanics/Geomechanics Symposium. pp. ARMA–05–810.

Haneberg, W.C., 1991. Pore pressure diffusion and the hydrologic response of nearly saturated, thin landslide deposits to rainfall. J. Geol. 99, 886–892.

Heap, M., Baumann, T., Gilg, H., Kolzenburg, S., Ryan, A., Villeneuve, M., Russell, J., Kennedy, L., Rosas-Carbajal, M., Clynne, M., 2021. Hydrothermal alteration can result in pore pressurization and volcano instability. Geology 49, 1348–1352.

Heap, M., Kennedy, B., Pernin, N., Jacquemard, P., Farquharson, J., Scheu, B., Lavallée, Y., Gilg, H., Letham-Brake, M., 2015. Mechanical behaviour and failure modes in the Whakaari (White Island volcano) hydrothermal system, New Zealand. J. Volcanol. Geotherm. Res. 295, 26–42.

Heap, M., Troll, V., Kushnir, A., Gilg, H., Collinson, A., Deegan, F., Darmawan, H., Seraphine, N., Neuberg, J., Walter, T., 2019. Hydrothermal alteration of andesitic lava domes can lead to explosive volcanic behaviour. Nat. Commun. 10, 5063.

Heise, W., Bannister, S., Williams, C.A., McGavin, P., Caldwell, T.G., Bertrand, E.A., Usui, Y., Kilgour, G., 2024. Magmatic priming of a phreatic eruption sequence: the 2012 Te Maari eruptions at Mt Tongariro (New Zealand) imaged by magnetotellurics and seismicity. Geophys. J. Int. 236, 1848–1862.

Hill, G.J., Bibby, H.M., Ogawa, Y., Wallin, E.L., Bennie, S.L., Caldwell, T.G., Keys, H., Bertrand, E.A., Heise, W., 2015. Structure of the Tongariro Volcanic system: Insights from magnetotelluric imaging. Earth Planet. Sci. Lett. 432, 115–125.

Hobden, B., Houghton, B., Davidson, J., Weaver, S., 1999. Small and short-lived magma batches at composite volcanoes: time windows at Tongariro volcano, New Zealand. J. Geol. Soc. 156, 865–868.

Hobden, B., Houghton, B.F., Lanphere, M., Nairn, I., 1996. Growth of the Tongariro volcanic complex: New evidence from K-Ar age determinations. N. Z. J. Geol. Geophys. 39, 151–154.

Hobden, B., Houghton, B., Nairn, I., 2002. Growth of a young, frequently active composite cone: Ngauruhoe volcano, New Zealand. Bull. Volcanol. 64, 392–409.

Hoek, E., 1968. Brittle fracture of rock. Rock Mech. Eng. Pr. 130, 9–124.

Hoek, E., 1994. Strength of rock and rock masses. ISRM News J. 2, 4–16.

Hoek, E., 2005. Uniaxial compressive strength versus Global strength in the Hoek-Brown criterion. Tech. Note RocNews, Vanc..

Hoek, E., Brown, E., 1980. Empirical strength criterion for rock masses. J. Geotech. Eng. Div. 106, 1013–1035.

Hoek, E., Brown, E., 1997. Practical estimates of rock mass strength. Int. J. Rock Mech. Min. Sci. 34, 1165–1186.

Hoek, E., Carranza-Torres, C., Corkum, B., 2002. Hoek-Brown failure criterion-2002 edition. Proc. NARMS- Tac 1, 267–273.

Hungr, O., McDougall, S., Wise, M., Cullen, M., 2008. Magnitude–frequency relationships of debris flows and debris avalanches in relation to slope relief. Geomorphology 96, 355–365.

Hurst, T., Jolly, A.D., Sherburn, S., 2014. Precursory characteristics of the seismicity before the 6 August 2012 eruption of Tongariro volcano, North Island, New Zealand. J. Volcanol. Geotherm. Res. 286, 294–302.

Hynes-Griffin, M.E., Franklin, A.G., 1984. Rationalizing the seismic coefficient method. Misc. Pap. GL- 84 13.

Iverson, R.M., 1995. Can magma-injection and groundwater forces cause massive landslides on Hawaiian volcanoes? J. Volcanol. Geotherm. Res. 66, 295–308.

John, D., Sisson, T., Breit, G., Rye, R., Vallance, J., 2008. Characteristics, extent and origin of hydrothermal alteration at Mount Rainier Volcano, Cascades Arc, USA: Implications for debris-flow hazards and mineral deposits. J. Volcanol. Geotherm. Res. 175, 289–314.

Jolly, A., Jousset, P., Lyons, J., Carniel, R., Fournier, N., Fry, B., Miller, C., 2014. Seismo-acoustic evidence for an avalanche driven phreatic eruption through a beheaded hydrothermal system: An example from the 2012 Tongariro eruption. J. Volcanol. Geotherm. Res. 286, 331–347.

Kennedy, B.M., Farquhar, A., Hilderman, R., Villeneuve, M.C., Heap, M.J., Mordensky, S., Kilgour, G., Jolly, A., Christenson, B., Reuschlé, T., 2020. Pressure controlled permeability in a conduit filled with fractured hydrothermal breccia reconstructed from ballistics from Whakaari (White Island), New Zealand. Geosciences 10, 138.

Kereszturi, G., Schaefer, L., Mead, S., Miller, C., Procter, J., Kennedy, B., 2021. Synthesis of hydrothermal alteration, rock mechanics and geophysical mapping to constrain failure and debris avalanche hazards at Mt. Ruapehu (New Zealand). N. Z. J. Geol. Geophys. 64, 421–442.

Kereszturi, G., Schaefer, L., Schleiffarth, W., Procter, J., Pullanagari, R., Mead, S., Kennedy, B., 2018. Integrating airborne hyperspectral imagery and LiDAR for volcano mapping and monitoring through image classification. Int. J. Appl. Earth Obs. Geoinf. 73, 323–339.

Lecointre, J.A., Neall, V., Wallace, C., Prebble, W., 2002. The 55-to 60-ka Te Whaiau Formation: a catastrophic, avalanche-induced, cohesive debris-flow deposit from Proto-Tongariro Volcano, New Zealand. Bull. Volcanol. 63, 509–525.

Leonard, G., Cole, R., Christenson, B., Conway, C., Cronin, S., Gamble, J., Hurst, T., Kennedy, B., Miller, C., Procter, J., 2021. Ruapehu and Tongariro stratovolcanoes: a review of current understanding. N. Z. J. Geol. Geophys. 64, 389–420.

Leroueil, S., 2001. Natural slopes and cuts: movement and failure mechanisms. Géotechnique 51, 197–243.

Marinos, P., Hoek, E., 2000. GSI: a geologically friendly tool for rock mass strength estimation. In: ISRM International Symposium. pp. ISRM–IS.

Matsui, T., San, K., 1992. Finite element slope stability analysis by shear strength reduction technique. Soils Found. 32, 59–70.

McGuire, W., 1996. Volcano instability: a review of contemporary themes. Geol. Soc. Lond. Spec. Publ. 110, 1–23.

Mick, E., Stix, J., de Moor, J.M., Avard, G., 2021. Hydrothermal alteration and sealing at Turrialba volcano, Costa Rica, as a mechanism for phreatic eruption triggering. J. Volcanol. Geotherm. Res. 416, 107297.

Mielke, P., Nehler, M., Bignall, G., Sass, I., 2015. Thermo-physical rock properties and the impact of advancing hydrothermal alteration—A case study from the Tauhara geothermal field, New Zealand. J. Volcanol. Geotherm. Res. 301, 14–28.

Miller, C., Kang, S., Fournier, D., Hill, G., 2018. Distribution of vapor and condensate in a hydrothermal system: Insights from self-potential inversion at Mount Tongariro, New Zealand. Geophys. Res. Lett. 45, 8190–8198.

Miller, C., Williams-Jones, G., 2016. Internal structure and volcanic hazard potential of Mt Tongariro, New Zealand, from 3D gravity and magnetic models. J. Volcanol. Geotherm. Res. 319, 12–28.

Mitchell, A., Allstadt, K.E., George, D., Aaron, J., McDougall, S., Moore, J., Menounos, B., 2022. Insights on Multistage Rock Avalanche Behavior From Runout Modeling Constrained by Seismic Inversions. J. Geophys. Res.: Solid Earth 127, e2021JB023444.

Moon, V., Bradshaw, J., Smith, R., de Lange, W., 2005. Geotechnical characterisation of stratocone crater wall sequences, White Island Volcano, New Zealand. Eng. Geol. 81, 146–178.

Mordensky, S., Heap, M., Kennedy, B., Gilg, H., Villeneuve, M., Farquharson, J., Gravley, D., 2019. Influence of alteration on the mechanical behaviour and failure mode of andesite: implications for shallow seismicity and volcano monitoring. Bull. Volcanol. 81, 1–12.

Mordensky, S., Villeneuve, M., Farquharson, J., Kennedy, B., Heap, M., Gravley, D., 2018a. Rock mass properties and edifice strength data from Pinnacle Ridge, Mt. Ruapehu, New Zealand. J. Volcanol. Geotherm. Res. 367, 46–62.

Mordensky, S., Villeneuve, M., Kennedy, B., Heap, M., Gravley, D., Farquharson, J., Reuschlé, T., 2018b. Physical and mechanical property relationships of a shallow intrusion and volcanic host rock, Pinnacle Ridge, Mt. Ruapehu, New Zealand. J. Volcanol. Geotherm. Res. 359, 1–20.

Mordensky, S., Villeneuve, M., Kennedy, B., Struthers, J., 2022. Hydrothermally induced edifice destabilisation: the mechanical behaviour of rock mass surrounding a shallow intrusion in andesitic lavas, Pinnacle Ridge, Ruapehu, New Zealand. Eng. Geol. 305, 106696.

Moretti, L., Allstadt, K., Mangeney, A., Capdeville, Y., Stutzmann, E., Bouchut, F., 2015. Numerical modeling of the Mount Meager landslide constrained by its force history derived from seismic data. J. Geophys. Res.: Solid Earth 120, 2579–2599.

Moretti, L., Mangeney, A., Capdeville, Y., Stutzmann, E., Huggel, C., Schneider, D., Bouchut, F., 2012. Numerical modeling of the Mount Steller landslide flow history and of the generated long period seismic waves. Geophys. Res. Lett. 39.

Nakagawa, M., Nairn, I., Kobayashi, T., 1998. The ~10 ka multiple vent pyroclastic eruption sequence at Tongariro Volcanic Centre, Taupo Volcanic Zone, New Zealand: Part 2. Petrological insights into magma storage and transport during regional extension. J. Volcanol. Geotherm. Res. 86, 45–65.

Okunishi, K., Okimura, T., 1987. Groundwater models for mountain slopes. In: Slope Stability: Geotechnical Engineering and Geomorphology. John Wiley & Sons New York, pp. 265–285, 17 Fig, 48 ref..

Pierson, T.C., Janda, R.J., Thouret, J.-C., Borrero, C.A., 1990. Perturbation and melting of snow and ice by the 13 november 1985 eruption of Nevado del Ruiz, Colombia, and consequent mobilization, flow and deposition of lahars. J. Volcanol. Geotherm. Res. 41, 17–66.

del Potro, R., Hürlimann, M., 2009. The decrease in the shear strength of volcanic materials with argillic hydrothermal alteration, insights from the summit region of Teide stratovolcano, Tenerife. Eng. Geol. 104, 135–143.

del Potro, R., Hürlimann, M., Pinkerton, H., 2013. Modelling flank instabilities on stratovolcanoes: parameter sensitivity and stability analyses of Teide, Tenerife. J. Volcanol. Geotherm. Res. 256, 50–60.

Procter, J., Cronin, S., Zernack, A., Lube, G., Stewart, R., Nemeth, K., Keys, H., 2014. Debris flow evolution and the activation of an explosive hydrothermal system; Te Maari, Tongariro, New Zealand. J. Volcanol. Geotherm. Res. 286, 303–316.

Pudasaini, S.P., Miller, S.A., 2013. The hypermobility of huge landslides and avalanches. Eng. Geol. 157, 124–132.

Qin, S., Jiao, J.J., Wang, S., 2001. The predictable time scale of landslides. Bull. Eng. Geol. Environ. 59, 307–312.

Reid, M., 2004. Massive collapse of volcano edifices triggered by hydrothermal pressurization. Geology 32, 373–376.

Reid, M., Sisson, T., Brien, D., 2001. Volcano collapse promoted by hydrothermal alteration and edifice shape, Mount Rainier, Washington. Geology 29, 779–782.

Revil, A., Murugesu, M., Prasad, M., Le Breton, M., 2017. Alteration of volcanic rocks: A new non-intrusive indicator based on induced polarization measurements. J. Volcanol. Geotherm. Res. 341, 351–362.

Rosas-Carbajal, M., Komorowski, J., Nicollin, F., Gibert, D., 2016. Volcano electrical tomography unveils edifice collapse hazard linked to hydrothermal system structure and dynamics. Sci. Rep. 6, 29899.

Roscoe, K., 1970. The influence of strains in soil mechanics. Geotechnique 20, 129–170.

Schaefer, L.N., Kendrick, J.E., Oommen, T., Lavallée, Y., Chigna, G., 2015. Geomechanical rock properties of a basaltic volcano. Front. Earth Sci. 3, 29.

Schaefer, L.N., Kereszturi, G., Kennedy, B.M., Villeneuve, M., 2023. Characterizing lithological, weathering, and hydrothermal alteration influences on volcanic rock properties via spectroscopy and laboratory testing: a case study of Mount Ruapehu volcano, New Zealand. Bull. Volcanol. 85, 43.

Shane, P., Maas, R., Lindsay, J., 2017. History of Red Crater volcano, Tongariro Volcanic Centre (New Zealand): Abrupt shift in magmatism following recharge and contrasting evolution between neighboring volcanoes. J. Volcanol. Geotherm. Res. 340, 1–15.

Sharma, R.H., 2013. Evaluating the effect of slope curvature on slope stability by a numerical analysis. Aust. J. Earth. Sci. 60, 283–290.

Sherburn, S., Bryan, C., Hurst, A., Latter, J., Scott, B., 1999. Seismicity of Ruapehu volcano, New Zealand, 1971–1996: a review. J. Volcanol. Geotherm. Res. 88, 255–278.

Siebert, L., 1984. Large volcanic debris avalanches: characteristics of source areas, deposits, and associated eruptions. J. Volcanol. Geotherm. Res. 22, 163–197.

Siebert, L., Glicken, T., 1987. Volcanic hazards from Bezymianny-and Bandai-type eruptions. Bull. Volcanol. 49, 435–459.

Siebert, L., Roverato, M., 2021. A historical perspective on lateral collapse and volcanic debris avalanches. In: Volcanic Debris Avalanches. Springer, pp. 11–50.

Siebert, L., Simkin, T., Kimberly, P., 2011. Volcanoes of the World. Univ of California Press.

Siratovich, P., Heap, M., Villeneuve, M., Cole, J., Kennedy, B., Davidson, J., Reuschlé, T., 2016. Mechanical behaviour of the Rotokawa Andesites (New Zealand): Insight into permeability evolution and stress-induced behaviour in an actively utilised geothermal reservoir. Geothermics 64, 163–179.

Sousa, J., Voight, B., 1995. Multiple-pulsed debris avalanche emplacement at Mount St. Helens in 1980: Evidence from numerical continuum flow simulations. J. Volcanol. Geotherm. Res. 66, 227–250.

Topping, W., 1974. Some Aspects of Quaternary History of Tongariro Volcanic Centre (Unpublished Ph.D. thesis). Victoria University, Wellington.

Van Asch, T., Malet, J., van Beek, L., Amitrano, D., 2007. Techniques, issues and advances in numerical modelling of landslide hazard. Bull. de la SociétÉ Géologique de Fr. 178, 65–88.

Van Duong, B., Fomenko, I.K., Nguyen, L.C., Nguyen, K.T., Do, T.-N., Gorobtsov, D.N., Zerkal, O.V., Dinh, H.T., 2023. Mathematical and numerical modeling of slope stability for the Mong Sen Landslide event in the Trung Chai Commune, Sapa, Vietnam. In: Progress in Landslide Research and Technology. vol. 2. Issue 1, 2023. Springer, pp. 193–207.

Van Wyk de Vries, B., Kerle, N., Petley, D., 2000. Sector collapse forming at Casita volcano, Nicaragua. Geology 28, 167–170.

Voight, B., Elsworth, D., 2000. Instability and collapse of hazardous gas-pressurized lava domes. Geophys. Res. Lett. 27, 1–4.

Wallace, C., Schaefer, L., Villeneuve, M., 2022. Material properties and triggering mechanisms of an andesitic lava dome collapse at Shiveluch Volcano, Kamchatka, Russia, revealed using the finite element method. Rock Mech. Rock Eng. 55, 2711–2728.

Walsh, F., Hochstein, M., Bromley, C., 1998. The Tongariro geothermal system (NZ): review of geophysical data. pp. 317–324.

Wong, F., 1984. Uncertainties in FE modeling of slope stability. Comput. & Struct. 19, 777–791.

Zhang, Y., Chen, G., Zheng, L., Li, Y., Zhuang, X., 2013. Effects of geometries on three-dimensional slope stability. Can. Geotech. J. 50, 233–249.

Zheng, H., Tham, L., Liu, D., 2006. On two definitions of the factor of safety commonly used in the finite element slope stability analysis. Comput. Geotech. 33, 188–195.

Zienkiewicz, O., Humpheson, C., Lewis, R., 1975. Associated and non-associated visco-plasticity and plasticity in soil mechanics. Geotechnique 25, 671–689.